MHD Mode Structure and Propagation in the ASDEX Device

O. Klüber, H. Zohm, H. Bruhns, J. Gernhardt,
A. Kallenbach, H.P. Zehrfeld

IPP III/140 Nov. 1989

MAX-PLANCK-INSTITUT FÜR PLASMAPHYSIK

8046 GARCHING BEI MÜNCHEN

MAX-PLANCK-INSTITUT FÜR PLASMAPHYSIK

GARCHING BEI MÜNCHEN

MHD Mode Structure and Propagation in the ASDEX Device

O. Klüber, H. Zohm, H. Bruhns, J. Gernhardt,
A. Kallenbach, H.P. Zehrfeld

IPP III/140 Nov. 1989

Die nachstehende Arbeit wurde im Rahmen des Vertrages zwischen dem Max-Planck-Institut für Plasmaphysik und der Europäischen Atomgemeinschaft über die Zusammenarbeit auf dem Gebiete der Plasmaphysik durchgeführt.

MHD Mode Structure and Propagation in the ASDEX Device

O. Klüber, H. Zohm, H. Bruhns, J. Gernhardt, A. Kallenbach,
H.P. Zehrfeld.

Max Planck-Institut für Plasmaphysik, EURATOM-Association,
D-8046 Garching.

Abstract.

In this paper, the Mirnov oscillations observed in the ASDEX tokamak are analyzed with regard to the generally accepted interpretation scheme according to which (1) Mirnov oscillations are caused by currents flowing parallel to $\underline{B}$ on rational magnetic surfaces and (2) the field perturbation is frozen within the plasma. If the second statement holds, the frequency is obtained from the profiles of the electron density, the ion temperature and an eventual toroidal or poloidal rotation velocity. It is shown that there are modes which follow this prediction. On the other hand, mode coupling is observed. Mode coupling is also invoked to reconcile the experimental findings with the predictions of a theory based on statement (1) according to which there is a poloidal variation of both the phase velocity and the amplitude of the Mirnov oscillations. While the observed phase velocity fits well into this picture, the poloidal variation of the amplitude cannot be ascribed to only one mode in the majority of cases. In addition, the possibility of coherent MHD activity due to currents in the scrape-off layer is discussed.

1.) Introduction

It is widely accepted that Mirnov oscillations with the poloidal and toroidal mode numbers m and n, respectively, are created by perturbating currents flowing parallel to the field lines on rational magnetic surfaces the q value of them being m/n. Furthermore, the field perturbation $\tilde{B}$ is expected to be frozen within the plasma, i.e. to move with a velocity which is simply the macroscopic velocity of the plasma as far as the single-fluid approximation is considered. In the two-fluid approximation the Hall term has to be taken into account, too, which introduces the electron drift velocity [1]. There is much qualitative but little quantitative experimental evidence which supports this interpretation scheme. It is the main aim of this paper to check the validity of these two fundamental statements, in particular the consequences arising from the toroidal geometry.

In a cylindrical plasma, the field perturbation would be of the type

$$\tilde{B}_\vartheta = \tilde{B}_\vartheta^{(o)} \cos (m\vartheta + n\varphi - \omega t). \qquad (1)$$

The toroidal curvature, however, leads to two substantial modifications: The slope of the magnetic field lines varies poloidally which results in a poloidal variation of the wavelength: it is larger at the outer (low field) side of the torus. This effect can be described in first order of the inverse aspect ratio by a transformation from ϑ to ϑ^*, namely

$$\vartheta^* = \vartheta - \lambda \sin \vartheta \qquad (2)$$

where $\vartheta = 0$ is in the midplane at the low field side. This transformation was first derived by Merezhkin [2] on the plausible assumption that the phase of the mode varies poloidally like the slope of the magnetic field lines of the resonant surface from which it originates. Shafranov's approximation leads to

$$\lambda = \left(\beta_p + \frac{l_i}{2} + 1 \right) \varepsilon \qquad (3)$$

where the values of β_p, the internal inductance l_i and the inverse aspect ratio $\varepsilon = r/R$ are those of the rational surfaces under consideration.

In the next section it will be shown that eq. (2) provides a sufficient description of the experimental findings. This is of particular technical importance for the MHD mode analysis in ASDEX since, due to the double-null divertor geometry, only half of the minor circumference could be equipped with Mirnov probes. Hence, even the determination of the poloidal mode number m is not obvious. In Section 2, after a brief description of the experimental setup, it is shown how this problem is solved.

The second toroidal effect is the poloidal variation of the perturbation amplitude $\tilde{B}_\vartheta^{(o)}$. Due to a quantitative treatment performed by one of the authors [3], this amplitude is expected to be larger at the torus outside. The underlying model - which obviously describes the phase variation, too - will be compared with experimental results in Section 4. Prior to performing this comparison, the propagation of the modes is discussed in Section 3. In the ASDEX device, beam-heated plasmas, in particular those with H-type confinement behaviour, were the favoured subject of MHD investigations [4 - 10]. Modes arising from major resonant magnetic surfaces (in the majority of cases differing in m by 1 while n = 1 for both of them) may propagate at different angular velocities and even in different directions. Such modes will be called "independent modes". On the other hand, n = 1 modes were observed with m = 1 and, e.g., m = 5, respectively, but exhibiting the same frequency. This phenomenon has been dubbed "mode coupling" and is ascribed to the mutual interaction of (at least) two perturbation currents flowing on rational surfaces differing in q = m/n, where one of them imposes its frequency onto the other one. On the basis of these experimental findings, in Section 4 the observed variety of poloidal asymmetries will be attributed to mode coupling.

Section 5 is dedicated to the investigation of two particular modes being characteristic for beam-heated ASDEX plasmas. In this connection, the possibility of perturbation currents flowing in the scrape-off layer will be discussed.

2.) Experimental Setup, Data Acquisition and Determination of the Poloidal Mode Number m.

In the original version, ASDEX was equipped with three poloidal sets of Mirnov probes located on circles at different toroidal positions. These sets are shown in Fig. 1 which demonstrates the essential handicap of mode analysis in a divertor tokamak: Only 102° at the low field side and 44° at the high field side are covered with Mirnov probes. (Here and in what follows, the angular distances are those between the centres of the probes.) In cylindrical geometry, i.e. at constant poloidal wavelength, these gaps would not matter at all; the angular distance of 7.3° between adjacent probes would allow for detecting poloidal mode numbers as large as 25. In a torus, however, the poloidal wavelength varies appreciably with ϑ; it is the smallest at the high field side of the torus where only 44° are accessible to observation. In 1986, the ASDEX divertor was reconstructed in order to stand more heat load due to the increased duration of the heating pulses. At this occasion, one of the three Mirnov probe sets had to be removed while another one was replaced by a set of newly designed probes which again cover 102° at the outer but now 61° at the inner side as shown in Fig. 2. For this set, the poloidal distance of the probes is 10.2°.

The data acquisition is done via CAMAC modules to a PDP 11-34 computer at a maximum sample rate of 250 kHz, which is 10 times the maximum observed signal frequency. 15 channels can be recorded with 24576 data points each, the time window available therefore being 100 ms. In case of low frequency phenomena, a sample rate of 50 kHz is sufficient, leading to a time window of about 500 ms.

The main topic of this paper is the analysis of Mirnov probe signals. It will be shown, however, that a comparison with the data obtained from the soft X-ray diodes is crucial for the interpretation in many cases. ASDEX is equipped with two SX cameras; one of them containing 33 diodes is viewing side-on, the other one with 25 diodes from above as indicated in Fig. 2. The data acquisition system is identical with that of the Mirnov probes; in parallel, the whole shot can be recorded at reduced data rate. Due to the presence of only two cameras, poloidal mode numbers $m > 2$ cannot be

determined by the system. In principle, m > 2 modes recorded by Mirnov probes may show up with the same frequency in the diode signals; usually however, the intensity arising from the near-boundary regions is too small. Hence, in most cases only m = 1 and m = 2 are detectable by the SX diodes.

As already mentioned in the introduction, the poloidal variation of the wavelength can be described in first order of the inverse aspect ratio by the Merezhkin transformation

$$\vartheta^* = \vartheta - \lambda \sin \vartheta. \qquad (2)$$

In ASDEX, it was found that eq. (2) describes well the observed variation of the poloidal wavelength in the sections where probes are located. In the following it is shown how eq. (2) can be used in order to determine the poloidal mode number m. In a limiter tokamak, the minor circumference is usually covered by equally spaced Mirnov probes. The poloidal mode number is then determined by plotting the $\dot{B}_\vartheta$ traces, taking a time slice and counting, e.g. the zeros as is demonstrated in Fig. 3 in which calculated signals are plotted for m = 3 and λ = 0.4 being typical for beam-heated plasmas. It is seen from this figure, that, due to the toroidal effect, there are phase shifts in the signals of the upper and lower probes. Hence, it is preferable to determine m by following e.g. a zero on its way around the minor circumference. According to eq. (2), this trace is not a line but an S-like contour.

Suppose now, that a fraction of the minor circumference is not equipped with Mirnov probes; this situation is indicated in Fig. 3 by the hatched sections. Apparently, the knowledge of the ϑ dependence of the wavelength (or phase velocity) according to eq. (2) helps to "jump across the gaps" in the appropriate way. If, according to the raw data, there is just one frequency, this procedure can be performed in a simple plot program; an example is shown in Fig. 4. A more sophisticated version is the fit of the data on the basis of eq. (2) resulting in the determination of m and λ with error bars. [11, 12,]. In order to perform that data analysis, points of equal phase (e.g. zeros) are determined and a least square fit to $\phi_i = m\,(\vartheta_i - \lambda \cdot \sin\vartheta_i) + \delta$ is done, where ϕ_i denotes the phase position of the i^{th} coil located at ϑ_i. λ, δ and m are free fit parameters, δ

accounts for the relative phase position. The optimal set of parameters λ, δ and m is found by minimizing

$$\chi^2 = \frac{1}{N-3} \sum_{i=1}^{N} (\phi_{if} - \phi_{io})^2 \qquad (4)$$

where ϕ_{io} and ϕ_{if} denote the measured resp. the fitted phase position. Usually m turns out to be close to an integer; for the fit it is allowed to be a REAL variable. This method can be applied to raw data or Fourier components; the latter is illustrated by Fig. 5 for an m = 6 mode. The fit delivers m = 5.96 and χ^2 = 0.04. For the sake of comparison, another fit is shown, too, with the parameters m = 3.7 and χ^2 = 0.6. Two time slices of this figure are shown in Fig. 6 in the form of polar diagramms which clearly demonstrate the degree of accuracy being available. For these plots, the amplitudes were fitted by a function of the type $a + b \cos \vartheta + c \sin \vartheta$.

Additional evidence is provided by following a field line or, to be more precise, a location of equal phase on its way around the major and the minor circumference. In the following, only the case n = 1 is considered. It is obvious, then, that for modes with even poloidal mode numbers (briefly called even modes) the probes located in the midplane at the outer and the inner side, respectively, are connected by a field line and are expected, therefore, to exhibit equal phases. Moreover, the outer and the inner part of a Mirnov probe set are partly connected to each other where the region of "overlap" is given by λ. For λ = 0.4, e.g., the ϑ^* interval of the outer probes is $\pm$ 33°, while that of the inner ones is $\pm$ 31° for the original version and $\pm$ 42° for the newly designed set. Thus, it is frequently possible to find pairs of outer and inner probes which are located at practically the same field line.

In the case of an odd mode number m, things become more complicated. We then take benefit, however, from the existence of more than one set of probes. This is demonstrated by Fig. 7, which is a map of the probe locations in the $\vartheta^* - \varphi$ plane for the present layout after modification. It is seen from this figure, that also for odd modes pairs or groups of probes can be found which are connected by a field line. The phase relations for the case depicted in Fig. 7 are shown in Fig. 8. Obviously, this procedure

can also be applied to even modes. It is always found that Mirnov probes located at the same field line exhibit the same phase. Hence, we arrive at the conclusion that eq. (2) provides a good description of the toroidal effect as far as the phase is concerned.

Finally, we have to say a few words on the toroidal mode number n. It is determined from those probes of the sets which are located in the midplane and several additional probes located in the midplane, too. This equipment is redundant by far since, apart from the occurrence of an m=3 / n=2 mode in the H regime, [8] no n>1 mode was ever observed.

3) Mode Propagation and Mode Coupling.

In this section, the motions of the mode structure and the signal frequencies arising from them are discussed. It is well known from elementary MHD theory, that a magnetic field created by currents flowing in a plasma tends to be frozen within it, i.e. it takes part in the motion of the plasma if the resistivity is sufficiently small. This is usually obtained from Maxwell´s equation $\nabla \times \underline{E} = -\partial \underline{B}/\partial t$ and generalized Ohm´s law in the single-fluid model $\eta \underline{j} = \underline{E} + \underline{v} \times \underline{B}$ where η and $\underline{v}$ are the resistivity and the velocity of the plasma, respectively. In the limit $\eta \rightarrow 0$, the combination of both equations leads to complete "freezing" of $\underline{B}$. In the two-fluid approximation, we obtain the mass velocity $\underline{v}$ and the current density $\underline{j}$ from the ion and electron velocities $\underline{v}_i$ and $\underline{v}_e$ by $\underline{v} = \underline{v}_i + m_e \underline{v}_e / m_i$ and $\underline{j} / (en_e) = \underline{v}_i - \underline{v}_e$. Generalized Ohm´s law reads then

$$\eta \underline{j} = \underline{E} + \underline{v} \times \underline{B} - \frac{1}{en_e} \underline{j} \times \underline{B} + \frac{1}{en_e} \nabla p_e \qquad (5)$$

where the last two terms are the Hall term and the electron pressure term. Applying the same procedure we find that the velocity at which the "frozen" field moves is a different one, namely

$$\underline{v}^* = \underline{v} - \frac{1}{en_e} \underline{j} - \frac{1}{en_e B^2} \nabla p_e \times \underline{B} . \qquad (6)$$

Note that the sum of the first two terms is just the electron velocity $\underline{v}_e$. We discuss now the contributions of the terms at the right-hand side of eq. (6) to $\underline{v}^*$ and start with the

electron drift velocity - $\underline{j}_\perp / (en_e)$. This velocity is essentially a toroidal one as can be seen from the equilibrium condition

$$\nabla p = \nabla (p_e + p_i) = \underline{j} \times \underline{B} \tag{7}$$

or, in cylindrical approximation

$$\frac{\partial p}{\partial r} = j_\vartheta B_\varphi - j_\varphi B_\vartheta \,. \tag{8}$$

In an ohmically heated ASDEX plasma the poloidal beta is of the order 0.3 which means that the contributions of j_ϑ and j_φ tend to cancel each other. This leads to the estimate

$$\frac{j_\vartheta}{j_\varphi} = \frac{B_\vartheta}{B_\varphi} \tag{9}$$

or, using

$$q = \frac{rB_\varphi}{RB_\vartheta} = \varepsilon \frac{B_\varphi}{B_\vartheta} \tag{10}$$

to

$$j_\vartheta = \frac{\varepsilon}{q} j_\varphi \,. \tag{11}$$

If signs are disregarded, eq. (11) holds also for the case of significant additional heating. In the case $\beta_p = 2$, e.g., the contributions of j_ϑ and j_φ to the pressure are again of the same order but now supporting each other (reversal of the sign of j_ϑ). Obviously, the term due to the electron pressure gradient does not alter the estimate given above since $p_e < p$. Thus we find that in the case $\underline{v} = 0$ the modes propagate with a velocity close to the electron drift velocity which is nearly toroidal. As far as the signal frequencies are concerned, however, even small poloidal velocities cannot be neglected: A pure toroidal drift velocity - $j_\varphi/(en_e) = \omega_\varphi R$ leads to the angular frequency $\omega_S = n\omega_\varphi$ of the Mirnov probe signal. The same frequency can be produced by a pure poloidal drift velocity - $j_\vartheta /(en_e) = \omega_\vartheta r$ if $\omega_S = m\omega_\vartheta$. From there we get

$$\frac{j_\vartheta}{j_\varphi} = \frac{r\omega_\vartheta}{R\omega_\varphi} = \frac{rn}{Rm} = \frac{\varepsilon}{q}$$

which coincides with eq. (11).

Substantial toroidal motion of the plasma is caused by the unidirectional tangential neutral injection. At a power level of 1 MW, the toroidal rotation velocity on axis is about 10^7cm s^{-1} which corresponds to an angular frequency of 2π x 10 kHz. The rotation velocity is more or less proportional to the heating power; the maximum values of the latter are 3.5 MW for H° and 4 MW for D° injection. The toroidal rotation velocity is measured via Doppler shift by charge exchange recombination spectroscopy [13]. Typical velocity profiles are parabolic or broader. Attempts were made to detect an eventual poloidal rotation of the plasma as it was observed in the near-boundary region of DIII - D [14]. Work is still in progress; so far, it can only be stated that a poloidal rotation velocity, if any, is below 10^6 cm s^{-1}.

In the ASDEX device, the plasma rotates in positive φ -direction, i.e. counter-clockwise if seen from above. Accordingly, in the case of counter-injection, both $\underline{v}$ and $-\underline{j}/(en_e)$ are in the same direction. This situation is illustrated in Fig. 9a where, as an example, the q = 3 surface is cut open and laid flat. In contrast, for co-injection, both motions oppose each other as shown in Fig 9b. Hence, it then depends on details what the resulting direction of $\underline{v}^*$ is.

Things become less complicated, if we regard a propagating MHD mode as a travelling wave. Accordingly its $\underline{k}$ vector is normal to the lines of equal phase which are the magnetic field lines of the rational surface from which the mode originates. Obviously, a motion parallel to $\underline{B}$ is irrelevant in the frame of this model. Hence, the vectors $\underline{v}$ and $\underline{j}$ of eq. (8) can be reduced to their components normal to $\underline{B}$ namely the normal velocity $\underline{v}_\perp$ and the diamagnetic electron drift velocity

$$-\frac{1}{en_e}\underline{j}_\perp = -\frac{1}{en_eB^2}\underline{B} \times (\underline{j} \times \underline{B}).$$

This leads to

$$\underline{v}^*_\perp = \underline{v}_\perp - \frac{1}{en_e}\underline{j}_\perp - \frac{1}{en_eB^2}\nabla p_e \times \underline{B}$$

or, taking into account eq. (9), to

$$\underline{v}_{\perp}^{*} = \underline{v}_{\perp} + \frac{1}{en_eB^2} \nabla p_i \times \underline{B}. \qquad (12)$$

According to this equation, the mode propagates with the sum of the normal macroscopic velocity and the reduced (∇p_i in lieu of ∇p) diamagnetic drift velocity. Both constituents are predominantly poloidal motions. Nevertheless, eqs. (6) and (12) are equivalent as far as the frequencies of the modes are concerned. Hence, we are free to establish a combination of them which is best suited for comparison with experimental data. We select

$$\underline{v}^{*} = \underline{v} + \frac{1}{en_eB^2} \nabla p_i \times \underline{B}. \qquad (13)$$

This equation can be directly derived from eq. (5) by substituting eq. (7). It allows for the determination of the mode frequency if the profiles of the electron density, the ion temperature and the toroidal rotation velocity are known. In order to give an estimate, what eq. (13) means for the signal frequency, we assume parabolic profiles for the ion temperature and the electron density. Then the absolute value of the second term becomes $2rkT_i(0) / eaB$ which means that the angular frequency of the motion is constant. $kT_i(0)$ is the ion temperature on axis. For $k\ T_i(0) = 1$ keV and $B = 2$ T we obtain $2.5 \cdot 10^5$ cm s^{-1} at $r = a$ and a signal frequency of m x 1.0 kHz. This has to be compared with the signal frequency created by the toroidal motion given above. Hence, near the boundary, where the toroidal rotation velocity is small, the contribution of the diamagnetic drift becomes competitive, in particular because of the weighting factor m/n.

An example is shown in Fig. 10. f_φ is the frequency due to the toroidal rotation of an L-type discharge obtained by co-injection. Hence, the frequency of the $m = 1 / n = 1$ mode is expected to be $f_\varphi - f_d$, where f_d is the frequency due to the reduced diamagnetic drift which is derived from the measured profiles of electron density and ion temperature. The location of the $q = 1$ surface is obtained from SX measurements; that of the $m = 2$ surface was estimated on the assumption that the total current flows within the $q = 2$ surface. This assumption overestimates to some extent the true radius

of the q = 2 surface. It is seen from Fig. 10 that $f_\varphi - 2f_d < 0$ which means that the m = 2 mode propagates in opposite direction, which agrees with the observation.

Fig. 10 presents an example for the simultaneous occurrence of two independent modes, i.e. modes propagating according to the local velocities. On the other hand, in many tokamaks mode coupling was observed, i.e. the simultaneous occurrence of two (or more) modes with different m/n ratio i.e. arising from different rational surfaces, but with same frequency [12, 15, 16, 17]. Obviously, the frequency can be ascribed to the local values of only one of the two (or more) rational surfaces. Therefore, we have to distinguish between driving and driven modes.

A very impressive example for mode coupling is presented in Figs. 11, 12 and 13. Fig. 11 depicts the temporal evolution of an H-type shot approaching the Troyon beta limit on a 150 ms time scale. Plotted are the poloided beta, the H_α/D_α emission from the upper divertor chamber indicating the occurrence of ELMs and the $\dot{B}_\vartheta$ traces from the Mirnov probes located at $\vartheta = 0$ and $\vartheta = \pi$, respectively. It is clearly seen that at t ~ 1.29 s an ELM occurs the amplitude of which (according to the H_α/D_α signal) exceeds appreciably those of the preceding and the successing ones. This particular ELM apparently triggers a different behaviour of MHD activity as far as $\dot{B}_\vartheta$ is concerned: it leads to the occurrence of a continuous mode. Fig. 12 is an expansion of Fig. 11 in a time window of 1.5 ms. In addition a signal of an SX diode viewing side-on near the midplane is plotted (cf. Fig. 2). According to Fig. 12, the sequence of events is as follows: Starting at t = 1.292 s, a low amplitude oscillation with a frequency of 28 kHz is seen in both the SX and Mirnov probe traces. Adding signals from other diodes and coils, we find m = 1/n = 1 for SX and m = 5/n = 1 for the Mirnov probes. Both modes propagate according to the toroidal velocity. At t = 1.2925 s, the amplitudes of the two signals rise up to 1.2926 s where, according to the H_α/D_α spike, a giant ELM occurs. (This is an example of fishbone-like MHD activity [4]. From Fig. 11, it might be inferred that such events are precursors to ELMs. In ref. [4], however, it was pointed out, that many ELMs are not preceded by "fishbones"). Immediately after that event, a mode develops which still propagates in the direction given by the toroidal rotation but at

appreciably reduced frequency, namely 8.5 kHz. From the Mirnov probe signals we obtain m = 2, n = 1. Furthermore, the previous oscillation has survived but with reduced amplitude. Again 5 ms later, the m = 2 mode imposes its frequency onto the SX signals which is shown in Fig. 13. The SX camera still shows an m = 1/n = 1 behaviour.

At the time when this discharge was performed, profiles of the toroidal rotation velocity were not yet taken; information from a region the major radius of which is roughly 195 cm, i.e. about 30 cm away from the magnetic axis was available. In this shot, the toroidal velocity v_t was $2.6 \cdot 10^7$ cm s^{-1} corresponding to f = 21 kHz.This is by a factor of 1.3 smaller than the frequency of the m=1 / n=1 mode which is located at a minor radius of ~13 cm. In this shot co-injection was applied, too, which means that the diamagnetic drift reduces the resulting frequency. Thus, for the fishbone-like event, the m=1 / n=1 mode is clearly the "master" i.e. driving the m=5 / n=1 oscillation. It was reported in previous papers [4, 8, 10] that in beam-heated ASDEX plasmas the m = 1/n = 1 mode may occur as precursor to sawtooth relaxations, as a quasi-stationary oscillation or as a fishbone-like event. Regardless on the waveform, there is always an n = 1 satellite with a rather large m number which means that the perturbation current is flowing near the separatrix. Most remarkably, mode coupling extends across the total plasma cross section in such cases. Similar observations were made at ISX-B [15] and TFTR [16]. For the latter device, MHD code simulations result in a cluster of coupled modes. In low q cases (corresponding to the common ASDEX operation regime), the m spectrum exhibits a pronounced maximum at m = 1, a minimum at m ~ 3 and then a continuous rise toward the boundary [16]. In ASDEX, such satellites exist also at combined neutral beam and ion cyclotron heating; they are not observed, however, if only ICRH is applied. Thus, the toroidal rotation caused by neutral injection appears to be a prerequisite for this type of mode coupling.

On the other hand, the observed frequency of the m=2 / n=1 mode which develops after the giant ELM is easily explained by the local rotation velocity at the q=2 surface diminished by the double frequency due to the drift term. Hence, we conclude that

after the occurrence of the ELM, the m=2 / n=1 oscillation imposes its frequency onto the m=1 / n=1 mode. This conclusion is supported by a more quantitative discussion as is shown by the frequency profiles of Fig. 14. In this figure, the profile f_φ of the toroidal rotation frequency is assumed to be half-circular, which corresponds to measured H-mode velocity profiles obtained in a later phase of ASDEX operation. The central value is chosen such that the measured velocity at r=30 cm is matched. The frequency f_d corresponding to the reduced diamagnetic drift velocity is obtained from profiles of the electron density n_e and the ion temperature T_i. A code simulation using the measured profiles delivers r=13 cm for this and r=33 cm for the q=2 surface. It is seen from Fig. 14 that the above assumption for f_φ is able to explain the experimental findings.

In the discharges shown in Figs. 10 and 14, the temperatures of electrons and ions are nearly equal. This means that the implementation of the complete (∇p in lieu of ∇p_i) diamagnetic drift velocity would impair the good agreement between the measured frequencies and those obtained from the profiles. Due to lack of information, we have neglected an eventual poloidal rotation of the plasma. At a minor radius of 32 cm, a velocity of $0.5 \cdot 10^6$ cm s^{-1} would contribute by 5 kHz to the signal frequency of the m = 2 mode and hence impair the agreement, too. We conclude, therefore, that in this region, i.e. at 3/4 of the minor radius, the poloidal rotation velocity, if any, is of the order 10^5 cm s^{-1} or smaller. Furthermore it is seen that the frequency of the m=1 mode can easily be compared with the experimental data while in the case of the m=2 mode it is much more sensitive to the accuracy of the profile determination. This holds the more for modes with m≥3 which are located near the separatrix, i.e. in a region for which reliable values of ∇p_i and v_φ cannot be obtained. For this reason, we are not able to provide quantitative evidence for the frequencies of m≥3 modes propagating in the direction of the diamagnetic electron drift [7]. It is very plausible, however, that the diamagnetic drift dominates the motion of the modes the more, the larger the poloidal mode number m is.

In the case of Figs. 12, 13 and 14, the direction in which the modes propagate is governed by the toroidal rotation which explains the occurrence of just one frequency: n=1 for all modes involved. Assuming a poloidal motion of two coupled modes, we would expect two frequencies according to the different poloidal mode numbers. This, however, was never observed in ASDEX nor - to the best kowledge of the authors - in other tokamaks while mode coupling, in particular between m=1 and m=2, is a quite usual phenomenon. As an example, such coupling occurs in some lower hybrid scenarios where the direction of propagation corresponds to the diamagnetic electron drift. Also in those cases, the frequency is the same for m=1 (SX) and m=2 (Mirnov probes). We conclude from this observation that the true motion of the mode structure is that given by eq. (6) which predicts an essentially toroidal velocity. Similar results were already obtained from Pulsator [17] . In Ohmic discharges it was observed that prior to disruptions the m=2 mode imposes its frequency onto the m=1 mode which was ascribed to a toroidal rotation of the mode structure.

The common feature of the examples discussed above is the coupling between the m=1 / n=1 mode detected by the SX diodes and an m >1 / n=1 mode detected by the Mirnov probes. It is tempting to conclude from this observation that the m=1 mode is particularly susceptible to mode coupling either by imposing its frequency onto a mode with larger m as in the case of Fig. 12 or by being dominated by a developing m=2 perturbation as in the case of Fig. 13. On the other hand, the occurrence of satellites to the m=1 mode contradicts to the widely accepted model of the m=1 internal kink according to which the perturbation is restricted to the interior of the q=1 surface at least in the cylindrical approximation. If toroidal effects are included, however, an m=2 component extending over the minor cross section is found [18].

As far as the interpretation of experimental data is concerned, we would like to point out that mode coupling is hard to detect if the modes manifest themselves in $\dot{B}_\vartheta$ signals only. As a simple example, a cluster of coupled modes with the mode numbers m - 1, m and m + 1 and the amplitudes $\gamma/2$, 1 and $\gamma/2$, respectively, is identical with a

mode having the mode number m and an amplitude varying like $1 + \gamma \cos \vartheta$ [11]. Thus, mode coupling might occur much more frequently than the first glance indicates.

Summarizing the outcomings of this section we arrive at the conclusion that the field perturbation $\tilde{B}$ propagates with the velocity predicted by theory and given by eq. (6) according to which $\underline{v}^*$ is a nearly toroidal motion. The dominant component of this vector parallel to $\underline{B}$, however, does not contribute to the measured value of $\tilde{B}_\vartheta$. Hence the signal frequency can be obtained by taking into account only the rather small component $\underline{v}^*_\perp$ normal to $\underline{B}$.

In giving this statement, we have disregarded the so-called mode locking which is due to the interaction between the moving mode structure and the image currents induced by it in the conductive wall. This effect becomes important if $\omega\tau$ approaches unity where ω is the angular frequency of the mode and τ the skin time of the vessel. The investigations on this topic performed in ASDEX are reported in another paper [19]. Here, only cases with $\omega\tau >> 1$ are discussed.

4) Modelling of Phase and Amplitude and Comparison with Experiment.

In Section 2, it was shown that eq. (2) provides a good description of the phase behaviour, if allowance is made for determination of λ from the experimental data rather than from Merezhkin´s formula, eq. (3). Furthermore, it was shown that the amplitude can be well fitted by $a + b \cos\vartheta + c \sin\vartheta$. Obviously, such fit can be replaced by a fit in ϑ^* which then leads to

$$\tilde{B}_\vartheta = (a_0 + a_c \cos \vartheta^* + a_s \sin\vartheta^*) \cos(m\vartheta^* + \delta) \qquad (14)$$

where the term $a_s \sin\vartheta^*$ allows for the observed up - down asymmetry of the amplitudes. Eq. (14) corresponds to the Fourier expansion

$$\tilde{B}_\vartheta = \sum_{i=-1}^{+1} a_{m+i} \cos(m+i)\vartheta^* + b_{m+i} \sin(m+i)\vartheta^* \qquad (15)$$

which means that the sidebands m-1 and m+1 are sufficient for a satisfactory fit. Nevertheless, eq (14) can be considered as describing a single mode with the

poloidal mode number m if we define such mode by having m maxima, m minima and 2m zeros. This is obviously fulfilled if the amplitude function has no zero, i.e. if $/a_c/</a_o/$ and $/a_s/</a_o/$. We ask now: Can a mode structure of this type be created by a perturbation current flowing on just one rational magnetic surface? In what follows we shall try to answer this question by comparing the experimental results to a model developed by Fussmann, Green and Zehrfeld [3] which deals with just this situation.

Prior to carrying out this comparison, we have to comment on the rather unexpected up-down asymmetry of the amplitudes: Regardless on the particular mode type, there is a clear up-down asymmetry, which was already seen from Figs. 4, 5 and 6. In some cases both on the outer and on the inner side of the torus, B_ϑ tends to increase with ϑ. More frequently, $|\tilde{B}_\vartheta|$ is larger at the upper than at the lower half of the torus. Such asymmetries are observed in well-positioned double-null configurations. As far as divertor action is concerned, a vertical displacement of $\pm$ 2cm is sufficient to provide a transition to effectively single-null operation which means that the double-null separatrix is split up such that only one of the divertor chambers is loaded by the particles and the heat leaving the main plasma. The up-down asymmetry of the mode amplitudes, however, is only marginally modified by the vertical position of the plasma.

The model of Fussmann, Green and Zehrfeld is also based on Shafranov's approximation but is going into more detail. The tokamak equilibrium is described by analytic functions for pressure and current, namely

$$p = p_o \left(1 - \frac{r^2}{a^2}\right)^\upsilon \qquad (16)$$

$$I(r) = I_p \left[1 - \left(1 - \frac{r^2}{a^2}\right)^{\mu+1}\right] \qquad (17)$$

where r is the minor radius of an inner magnetic surface, a that of the plasma column, I_p the total toroidal current and p_o the pressure at the magnetic axis. For integer values

of μ and ν, analytic solutions of the Grad-Shafranov equation are obtained. It is supposed now that on a rational magnetic surface q=m (n=1 assumed) a perturbation surface current is flowing parallel to the magnetic field lines giving rise to a magnetic field perturbation $\tilde{B}$. The superposition of $\tilde{B}$ and the equilibrium field leads to the creation of magnetic islands at that and at the neighbouring rational surfaces characterized by m-1 and m+1.

On the basis of this model, $\underline{\tilde{B}}$ outside the plasma is calculated. An example is shown in Fig. 15, namely a polar diagram of $\tilde{B}_\vartheta$ for the case $\beta_p = 1.5$, m = 4. It is clearly seen that the poloidal wavelength decreases appreciably from the outer to the inner side. So does the amplitude but not monotonically: the upper and lower maxima exceed that in the midplane at the outer side. Apparently we cannot compare this particular feature with the experiment since this is just the region where no Mirnov probes are located. In our calculation, the major radius of the plasma is assumed to be R_p = 168 cm; the centre of the circle defined by the Mirnov probe sets is also 168 cm apart from the torus axis. Obviously, the precise value of R_p enters into the amplitudes and marginally also into the phases of the field pertubation.

We first compare the behaviour of the phase with that predicted by eqs. (2) and (3). For this purpose, we refer to a situation analogous to $\underline{\tilde{B}}_\vartheta \propto \sin(m\vartheta)$, i.e. $\underline{\tilde{B}}_\vartheta(\pi) = 0$. With incrasing ϑ, the next zeros are found at ϑ_o (outside) and ϑ_i (inside). We define now λ_o and λ_i by

$$m(\vartheta_o - \lambda_o \sin \vartheta_o) = \pi,$$

$$m(\pi + \vartheta_i - \lambda_i \sin \vartheta_i) = \pi.$$

These two values and the average of them can be compared with λ_M according to eq. (3). The result of such a comparison is listed in Table 1.

μ	m	$\frac{r_{res}}{a}$	$\frac{l_i}{2}$	λ_o	λ_i	$\frac{\lambda_o + \lambda_i}{2}$	λ_M
3	3	0.94	0.72	0.45	0.79	0.62	0.72
4	4	0.97	0.82	0.43	1.03	0.73	0.77
5	5	0.99	0.90	0.41	1.20	0.80	0.80

Table 1: Phase asymmetry parameters for $\beta_p = 1.5$, $\nu = 2$. r_{res} is the minor radius of the resonant surface, a that of the plasma column. The meaning of the other quantities is explained in the text.

For the sake of simplicity, the current distribution parameter μ was chosen such that the perturbation current is flowing near the plasma boundary, which, assuming a central q value of 0.85, is achieved by choosing $\mu = m$. Accordingly, the Merezhkin parameter λ_M given by eq. (3) is calculated from the values of β_p and $l_i / 2$ at $r = a$. It is seen from this table that λ_0 and λ_i differ appreciably from each other while $(\lambda_0 + \lambda_i) / 2$ comes close to λ_M. From the data of Table 1, one gets the impression that eq. (2), assuming a constant λ (not varying with ϑ) might be a rather unsatisfactory approximation. What such variation of λ really means, however, is demonstrated by Fig. 16. In this figure, $\tilde{B}_\vartheta$ calculated from the model for the case $m = 3$, $\mu = 3$, $\beta_p = 1.5$ is plotted. This curve is compared to that obtained from a calculation of $\tilde{B}_\vartheta$ according to eqs. (2) and (3) where $\lambda = 0.62$ (cf. Tab. 1) and where the amplitude is chosen arbitrarily. It is seen from this figure that the assumption of a λ value not varying with ϑ does not lead to appreciable phase errors as compared to those arising from experimental ones. Hence, eqs. (2) and (3) are justified by the model calculation.

Obviously, the model provides amplitudes symmetric to the midplane. Furthermore, the above mentioned non-monotonic behaviour of the calculated amplitudes cannot be compared with that of the measured ones. Thus, we have to restrict the comparison to the out-in-contrast of the mode amplitudes. The most simple measure of it is the ratio ρ_m of the probes located in the midplane at the low-field and the high-field side of

the torus, respectively. $\rho_m > 1$ means that the amplitude is larger at the outer side. In lieu of this quantity the out-in ratio ρ_a of the averaged signals from both parts of the probe sets can be considered. In general, both quantities do not deviate appreciably from each other; hence, in the following we sometimes refer to ρ without specifying what particular quantity is meant. It should be mentioned that, obviously, there is some influence of the particular horizontal position of the plasma column onto the out-in ratio of the mode amplitudes. Due to the divertor configuration and the dimensions of the discharge chamber, divertor operation is possible at major radii between 164 and 170 cm, (168 cm being the major radius of the Mirnov probe circles) while the minor horizontal diameter 2a does not depend on R but slightly on $\beta_p + l_i/2$. For OH plasmas, this value is typically 1 which leads to 2a = 80 cm. With increasing β_p, 2a may amount up to 85 cm. The observed variety of contrast ratios, however, is far from being attributable to the variation of R or a.

In Table 2, some representative values of ρ_m, the out-in amplitude ratio in the midplane, are listed. It is clearly seen that ρ_m increases with both the poloidal β and the poloidal mode number m. It should be noted that $\beta_p = 2$ is approximately the maximum value achievable at approaching the Troyon beta limit. On the other hand, $\beta_p = 0.1$ is unrealistically small; it has been taken into this table, however, in order to demonstrate the influence of the poloidal beta onto the amplitude ratio.

β_p	m	$\rho_m(2)$	m	$\rho_m(3)$	m	$\rho_m(4)$
0.1	2	1.5	3	1.6	4	1.9
0.5	2	1.8	3	1.8	4	2.7
1.0	2	2.2	3	2.5	4	4.3
1.5	2	2.7	3	3.5	4	7.6
2.0	2	3.3	3	5.6	4	17.2

Table 2: ρ_m, the out-in amplitude ratio of $\tilde{B}_\vartheta$ as a function of m and β_p. $\mu = 3$ in the cases m = 2 and m = 3, $\mu = 4$ for m = 4. $\upsilon = 2$ for all profiles.

Out of all Mirnov oscillations, the m=2 / n=1 mode observed at quite different scenarios [8] comes closest to the theoretical expectations, i.e. the measured values of ρ agree frequently with the predicted ones. There are, however, cases where ρ is slightly smaller than 1 which, according to the model, should never occur. This trend is reinforced for the m≥3 / n=1 mode propagating in the electron diamagnetic drift direction in beam-heated plasmas [7]. For this mode the cases with $\rho \sim 1$ prevail. In contrast, for the satellite of the m = 1 mode (see refs. [4, 8, 10]), $\rho \sim 1$ is found only in very rare cases. Usually ρ is not only larger than unity; moreover, it frequently exceeds by far the conceivable values according to our model. Contrast ratios as large as 25 have been found even at moderate values of β_p; this figure, however, is not an upper limit since in many cases the signals from the inner part of the probe set are undetectably small. In general, for all mode types the behaviour of ρ is very erratic; in particular it is not correlated to quantities as e.g. mode number or poloidal beta.

Thus we are confronted with the fact that , while predicting the behaviour of the phases satisfactorily well, our model is not able to describe even roughly that of the amplitudes. Of course, we have to require that both the phase and the amplitude are modelled, which follows from a very simple consideration: Let $\underline{j}_t$ be the perturbation current and $\underline{B}$ the unperturbed magnetic field. Our model claims

$$\underline{j}_t = \alpha \underline{B} \tag{18}$$

where α is a scalar function. We have to postulate div $\underline{j}_t = 0$, i.e.

$$\underbrace{\alpha \operatorname{div} \underline{B}}_{=0} + \underline{B} \operatorname{grad} \alpha = 0 \tag{19}$$

which is only fulfilled if α does not vary along a field line of the unperturbed magnetic field. Hence, the out-in-contrast of the amplitude $\tilde{B}_\vartheta^{(o)}$ cannot deviate drastically from that of $\underline{B}$.

On looking out for a modification of our interpretation scheme which saves the basic idea but conforms to the experimental findings, our attention is drawn to the empirical fact of mode coupling. Two examples were already discussed in Section 3 and it was

mentioned there that mode coupling is a quite common feature of tokamak plasmas. This holds not only for the coupling between the modes m = 1 and m = 2 but also for the "satellites" of the m = 1 with large m number as e.g. 5. As stated in ref. [8], m = 1 modes in beam-heated ASDEX plasmas are always observed to be accompanied by such satellites regardless on the waveform, i.e. sawtooth precursor, continuous mode or fishbone-like burst.

On the basis of these observations, we feel justified to propose mode coupling as the most conceivable explanation for the observed variety of out-in amplitude ratios. Since the measured amplitudes can be well fitted by three modes with constant amplitudes (cf. eq. (15)) the superposition of the fields of three neighbouring modes according to the model is expected to be sufficient, too. Obviously, the proposed interpretation scheme allows also for up-down asymmetries of the amplitudes which can be obtained from phase differences between the three substituents.

As a first example, we present the simulation of the m = 6 mode already shown in Fig. 6. For the sake of better comparison, Figs. 17b and 17e are a repetition of the two time slices of Fig. 6. The dominant component m = 6 is plotted in Figs. 17a and 17d. The out-in ratio of its amplitude is smaller than the measured one; hence in the simulation the maxima coincide (apart from the phase shift) at the low-field side of the torus. Figs. 17c and 17f are obtained by superimposing the modes m = 5 and m = 7 with the relative amplitude 0.20 for the perturbation currents of both sidebands. The up-down asymmetry is due to a phase shift of $\pm 23^{\circ}$ relative to the leading mode. It is seen from this figure that sidebands with moderate amplitudes and phase shifts are sufficient to account for the out-in and the up-down asymmetries. Another simulation is shown in Fig. 18. In this case the out-in ratio of the leading mode is larger than the measured one so that the maxima have to couple at the inner side. The relative amplitude of the sidebands is 0.22 while the phase shift is $\pm 8^{\circ}$. Note that in both cases the fairly good agreement was achieved without fully utilizing the number of free parameters: The amplitudes of the sideband currents might differ and there is no need to assume that

the phase shifts are opposite in sign but equal in absolute value. These restrictions were introduced by the authors just for reducing complexity.

Thus we have found that the concept of perturbation currents flowing on rational magnetic surfaces leads to satisfactory agreement with the experimental observations obtained from ASDEX - and presumably from other devices, too - if allowance is made for the coupling of at least three modes with the mode numbers m-1, m and m+1, respectively, produced by currents flowing on the according rational magnetic surfaces.

5.) Problems and indications for quasi-resonant mode coupling.

So far, mode coupling was defined as the interaction of at least two perturbation currents flowing on different rational surfaces. This type of mode coupling is a resonant one since the perturbation field of a single current distribution with the mode number m contains also components with all other mode numbers, in particular m-1 and m+1. On the other hand, as already stated before, a field perturbation $\tilde{B}$ induces currents in all surrounding conductors if there is a relative motion between them. (The most prominent example is the so-called mode locking i.e. the interaction of a moving mode with the currents induced by it in the vessel wall). Hence, there might also be some interaction between the plasma inside the separatrix and the scrape-off layer.

We follow this idea because we are obliged to explain a rather puzzling observation. In Section 3 and ref. [8], the satellite to the m = 1 mode was discussed. It was found that its poloidal mode number m_s is always exceeding the boundary q value

$$q' = \frac{2\pi a^2 B_\varphi}{\mu_o R_o I_p}\left[1 + \varepsilon^2\left\{1 + \frac{1}{2}\left(\beta_p + \frac{l_i}{2}\right)^2\right\}\right] \qquad (20)$$

which takes into account the toroidal curvature but disregards the contribution of the multipole coils. As a rule m_s is the smallest integer number which exceeds q′. Obviously, q is singular at the separatrix and hence rational surfaces with arbitrarily large m/n ratio can be found within it. In the ASDEX device, the divertor coil triplets are designed such that the field produced by them has a very short range. This is seen from Fig. 1 which shows that the deviation of a near-circular boundary is restricted to the immediate environment of the stagnation point. This means that the q values of magnetic surfaces located a few cms inside the separatrix are practically equal to those of a limiter tokamak. This is demonstrated quantitatively by Fig. 19 which is a plot of q versus the minor radius r (more precisely: $r = R-R_0$), for both a divertor and a limiter configuration. It is seen from this figure that inside the separatrix the q values do not begin to differ from each other except at the last two centimeters. Outside the separatrix, however, the q values of both configurations differ appreciably due to the enhanced poloidal way of the field lines in the divertor case.

In this calculation, an ideal separatrix was assumed. The real magnetic configuration, however, will be disturbed by the unavoidable imperfections of the divertor coils: They might be somewhat elliptical, their centres need not be located precisely on the same vertical axis and they may be slightly tilted. Model calculations performed by Neuhauser [20] have shown that deviations of a few mm lead to appreciable ergodization of the near-separatrix region. As a consequence, closed magnetic surfaces with arbitrary large q values are not realized. For this reason it is questionable whether or not the satellite current is flowing inside the separatrix.

In previous papers [7, 9] it was reported that in L-type beam-heated ASDEX plasmas and in the L phase preceding L-H transitions an $m \geq 3 / n = 1$ mode is frequently found which propagates in the direction of the electron diamagnetic drift (i.e. opposite to the satellite mode). Usually, this mode occurs simultaneously with the satellite oscillation. Thus both modes have to be separated by Fourier decomposition. The number m* of the localized mode is always smaller than the q′value according to eq. (20) which means that the perturbation current of this mode is clearly flowing inside the

separatrix. As a rule, m^* is the largest integer number being smaller than q'; hence, this mode is located close to the separatrix. Combining this statement with that given on the mode number m_s of the satellite, we arrive at the relation

$$m_s = m^* + 1 \qquad (21)$$

which holds for all cases analyzed so far. This statement has to be qualified: In ASDEX, beam-heated discharges with $q' > 5$ were but occasionally produced and not investigated in detail. Hence, m_s ranges between 3 and 5 only, where $m_s = 3$ is observed at $q' < 3$. In such discharges an $m = 2$ mode is observed, which propagates in the direction of the diamagnetic electron drift; an example was shown in Fig. 10. Including such modes, m^* ranges between 2 and 4 according to eq. (21). There is, however, a significant difference between $m^* = 2$ on the one and $m^* = 3$ or 4 on the other hand. While modes with $m^* = 3$ or 4 occur only in the L-regime and during ELMs a quasi-stationary $m = 2$ mode propagating in the direction of the diamagnetic electron drift is observed regardless on the particular heating scheme provided that q' is sufficiently close to 2 which in practice means $q' < 2.5$. For this reason, the underlying physics are likely to be different in the case $m^* = 2$.

Considering the interpretation scheme being established in the preceding section, we are confronted to the following problems: So far, it was tacitly assumed that the sideband modes $m - 1$ and $m + 1$ are always "available" which means that the according resonant surfaces are located inside the separatrix. As far as the m^* mode is concerned, it is questionable whether or not the sideband $m^* + 1$ can be realized by a current flowing at a closed resonant surface inside the separatrix. In the case of the satellite mode, this is even not clear with respect to the main component.

There are some experimental indications for the possibility of Mirnov oscillations caused by currents flowing outside the separatrix. The most impressive one is obtained by a moveable Mirnov probe which was introduced into the upper divertor as shown in Fig. 2. The $\dot{B}_\vartheta$ signals of this probe exhibit always the frequency of the satellite oscillation while that of the m^* mode - if detectable at all - is very weak. Furthermore, the frequency of the satellite shows up in the signals of Langmuir probes

which are positioned in the scrape-off layer while that of the m^* mode is never seen. This holds also for the signals of other diagnostics, e.g. for reflectometry probing the scrape-off layer.

Thus we have to cope with the eventual occurrence of perturbation currents flowing outside the separatrix. The patterns of such currents may close in the same way as image currents do at the gaps of a conducting vessel, namely by connecting a region of positive current with the neighbouring region of negative current. Apparently, this scheme works well if these currents are still flowing on rational magnetic surfaces, except for the "connecting" region. For this reason, we consider this kind of mode coupling as a quasi-resonant one. The perturbation currents in the scrape-off layer may be shorted by the divertor plates which would explain the large amplitudes recorded by the Mirnov probe positioned in one of them.

Obviously, we are not able to determine the true mode number of a mode caused by currents in the scrape-off layer since the spatial structure of the $\tilde{B}_\vartheta$ signals reflects only that of the equilibrium configuration in the main chamber which - as stated above - deviates from circular magnetic surfaces only near the stagnation points.

Finally, another puzzling feature of the satellite mode should be mentioned: In some cases, all signals from the probes positioned at the high-field side are practically in phase while those from the low-field side exhibit the usual pattern of a travelling wave. An example is shown in Fig. 20. Apparently, such behaviour can be ascribed to the superposition of an m = 0 / n = 1 mode. Indeed, by subtracting the average of all signals amplitudes from each individual signal, a travelling mode is reconstructed for the inner section, too. It is difficult to comment on this observation since the occurrence of the m = 0 component cannot be attributed to quantities like q, β_p or others which might be thought to be relevant for this phenomenon.

6. Summary

The basic concept of helical perturbation currents flowing on rational magnetic surfaces as the source of Mirnov oscillations is examined by comparing a quantitative model based on Shafranov's approximation with the experimental data obtained on ASDEX in order to describe quantitatively the measured poloidal asymmetries of phase and amplitude. As far as the phase is concerned, satisfactory agreement was found. The observed behaviour of the amplitudes can be reconciled with this concept, too, if mode coupling is invoked. The assumption of two sidebands is sufficient to simulate the experimental findings. The discussion of two particular modes leads to the consideration of perturbation currents eventually flowing in the scrape-off layer. Experimental evidence for such currents is given.

Apart from the poloidal structure of the mode, its propagation, say the frequency of the $\dot{B}_\vartheta$ signal, calls for explanation. This is based on the concept of frozen magnetic fields. In the past, there was some discussion whether particular modes propagate in toroidal or in poloidal direction. This question cannot be decided from experimental data since only the component normal to $\underline{B}$ enters into the signal frequency. At the first glance, the existence of coupled modes arising from different magnetic surfaces and expected to have different frequencies appear to enhance the confusion. In contrast, as is shown in this paper, this phenomenon clarifies the situation: MHD modes in Tokamaks propagate in nearly toroidal direction.

Acknowledgements

The authors acknowledge with appreciation the impact arising from the work done by K. Toi (Nagoya University) and S. von Goeler (Princeton University) during their stays at IPP Garching. Furthermore, they are indebted to their colleagues in the ASDEX team for continuous support, in particular to G. Becker, R. Büchse, A. Carlson, H.-U. Fahrbach, L. Giannone, K. Grassie, W. Herrmann, M. Kornherr, K. McCormick, J. Neuhauser, A. Rudyj and F. Wagner. I. Mustapic gave valuable assistance by implementing important evaluation tools on the computer.

References

[1] Glenn Bateman,
MHD Instabilities,
The MIT Press, Cambridge, Massachusetts and London, England

[2] V.G. Merezhkin,
Sov. J. Plasma Phys. 4 (1978) 152.

[3] G. Fussmann, B.J. Green, H.P. Zehrfeld,
in Plasma Physics and Controlled Nuclear Fusion Research 1980 (Proc. 8th Int. Conf. Brussels 1980) Vol 1, IAEA, Vienna (1981) 353.

[4] O. Klüber, J. Gernhardt, K. Grassie et al.
in Controlled Fusion and Plasma Heating (Proc. 13th Eur. Conf. Schliersee 1986) Vol 10C, Part I, European Physical Society (1986) 136.

[5] O. Gruber, G. Becker, G. von Gierke et al.
in Plasma Physics and Controlled Nuclear Fusion Research 1986 (Proc. 11th Int. Conf. Kyoto 1986) Vol 1, IAEA Vienna (1987) 357.

[6] K. Grassie, O. Gruber, O. Klüber et al.
in Controlled Fusion and Plasma Heating (Proc. 14th Eur. Conf. Madrid 1987) Vol 11D, Part I, European Physical Society (1987) 226.

[7] K. Toi, J. Gernhardt, O. Klüber, M. Kornherr,
Phys. Rev. Lett., Vol 62 (1989) 430.

[8] O. Klüber, J. Gernhardt, S. von Goeler, M. Kornherr, K. Toi, H.P. Zehrfeld
in Controlled Fusion and Plasma Physics (Proc. 16th Europ. Conf. Venice 1989) Vol 13B, Part II, European Physical Society (1989) 473.

[9] S. von Goeler, O. Klüber, G. Fussmann, J. Gernhardt, M. Kornherr,
MHD Activity during ELMs, submitted for publication to Nucl. Fusion.

[10] ASDEX Team, The H-Mode of ASDEX
submitted for publication to Nucl. Fusion.

[11] G. Hammett, K. McGuire,
Analysis of Mirnov Oscillations on PDX, Rep. PPPL-1854, Princeton Plasma Physics Laboratory, Princton NJ (1982)

[12] T. Harley, D. Buchenauer, J. Coonrod, K. McGuire,
TFTR Mirnov Coil Analysis at Plasma Start-up, Rep. PPPL-2298, Princeton Plasma Physics Laboratory, Princeton NJ (1986)

T.R. Harley, D.A. Buchenauer, J.W. Coonrod, K.M. McGuire,
Nucl. Fusion 29 (1989) 771.

[13] A. Kallenbach, H.M. Mayer, K. Brau et al,
in Controlled Fusion and Plasma Physics (Proc. 16th. Europ. Conf. Venice 1989) Vol 13 B, Part I, European Physical Society (1989) 175.

[14] R.J. Groebner, P. Gohil, K.H. Burrell, T.H. Osborne, R.P. Seraydarian, H.St. John,
in Controlled Fusion and Plasma Physics (Proc. 16th. Europ. Conf. Venice 1989) Vol 13 B, Part I, European Physical Society (1989) 245.

[15] J.L. Dunlap, B.A. Carreras, V.K. Paré et al,
Phys. Rev. Lett. 48 (1982) 538.

[16] J. Manickam, V. Arunasalam, M.G. Bell et al.,
Stability of TFTR Plasmas, to be published in Plasma Physics and Contr. Nucl. Fusion Research (Proc. 12th Int. Conf. Nice 1988), IAEA-CN-50 / A-VII-4.

[17] F. Karger, K. Lackner, G. Fussmann et al,
Plasma Physics and Contr. Nucl. Fusion Research (Proc. 6th Int. Conf. Berchtesgaden 1976) Vol I, IAEA Vienna (1977) 267.

[18] M.N. Bussac, R. Pellat, D. Edery, J.L. Soule,
Phys. Rev. Lett. 35 (1975) 1638.

[19] H. Zohm, A. Kallenbach, H. Bruhns, G. Fussmann, O. Klüber,
Plasma angular momentum loss by MHD mode locking, submitted for publication to Europhys. Lett.

[20] J. Neuhauser, M. Bessenrodt-Weberpals, B.J. Braams et al.,
in Controlled Fusion and Plasma Physics (Proc. 16th Europ. Conf. Venice 1989),
31 (1989) 1551

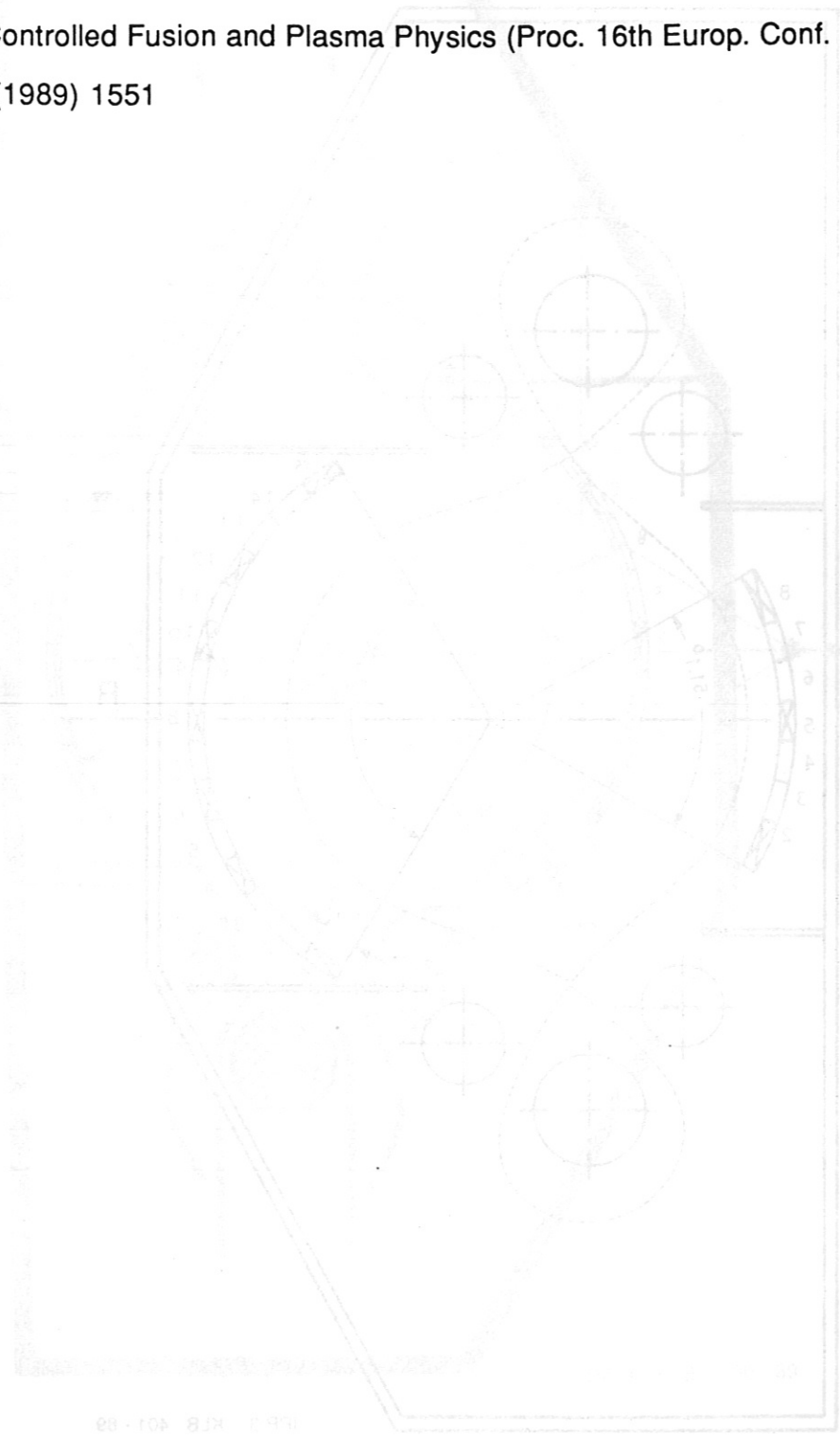

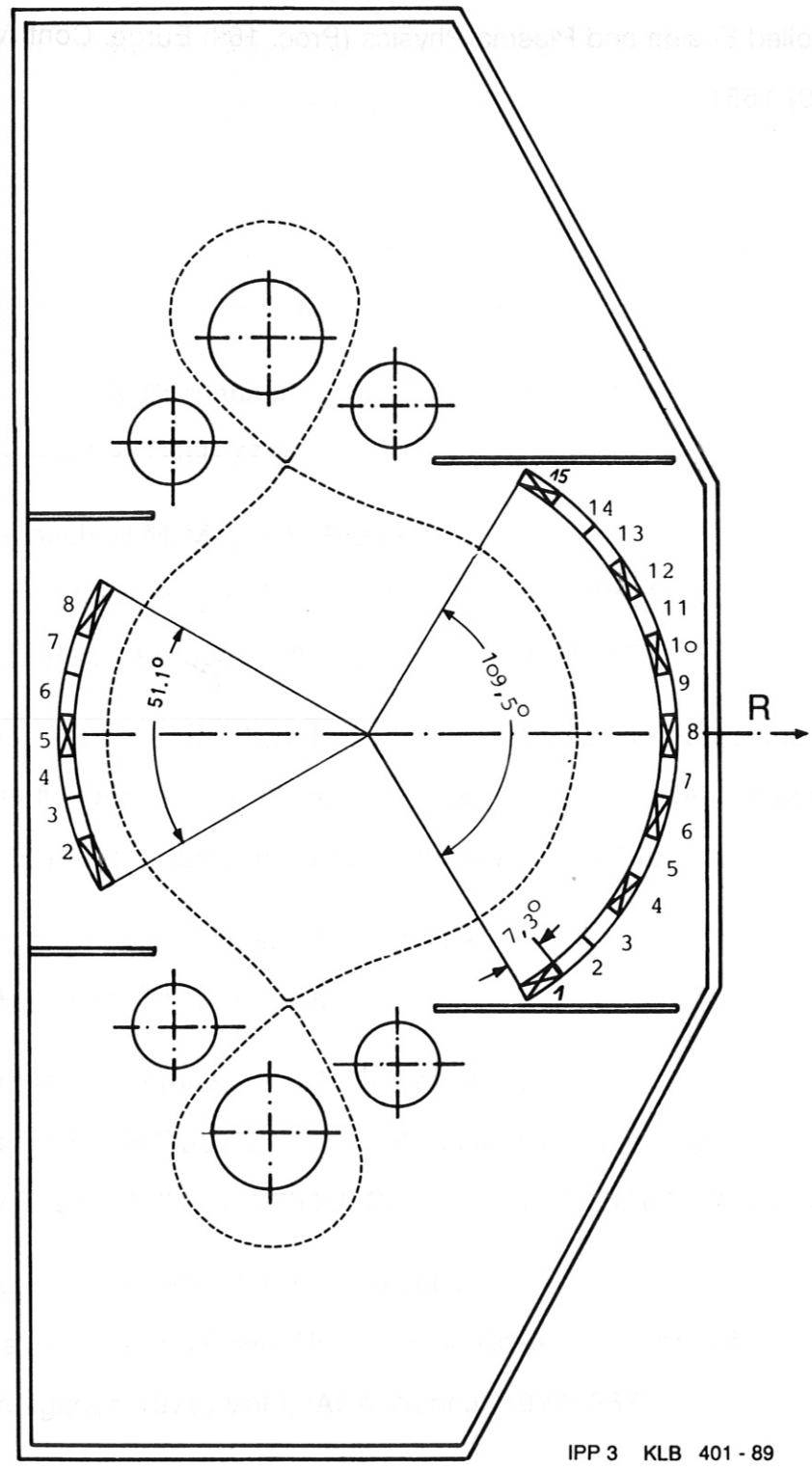

Fig. 1 Mirnov probe array, original version. Usually, the signals from the probes marked by crosses were recorded. The signal names A 1 WNW to A 15 WNW (outer section) and I2WNW to I8WNW (inner section) quoted in some of the following figures refer to such an array. For the sake of comparison, the separatrix (dashed line) is shown, too.

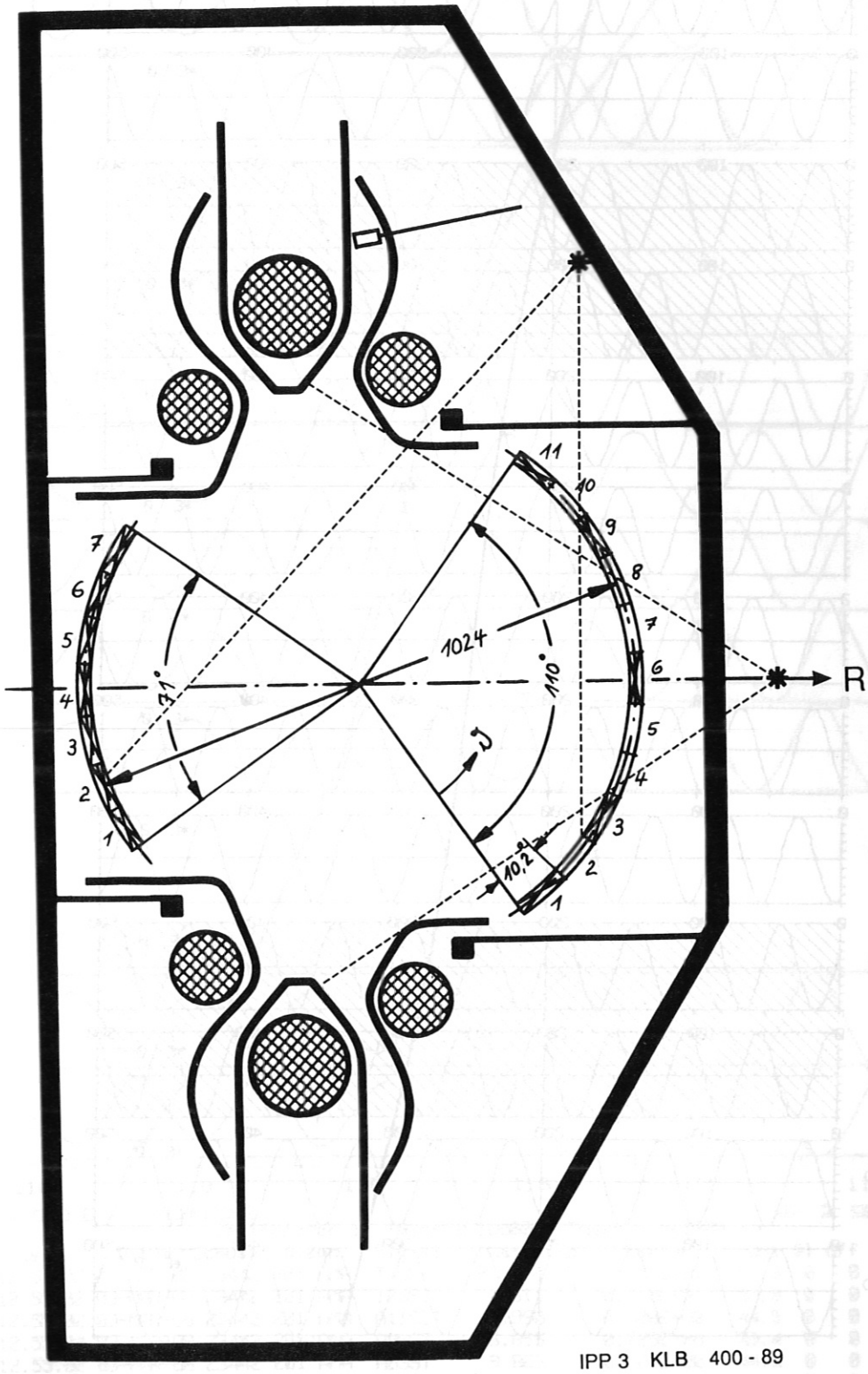

Fig. 2: Mirnov probe array, recent version. Usually, the signals from the probes marked by crosses were recorded. The signal names A1SST to A11SST (outer section) and I1SST to I7SST (inner section) quoted in some of the following figures refer to this array. In some cases, a moveable magnetic probe was introduced into the upper divertor chamber. The dashed lines indicate the field of vision of the SX diode cameras (located in a different poloidal plane).

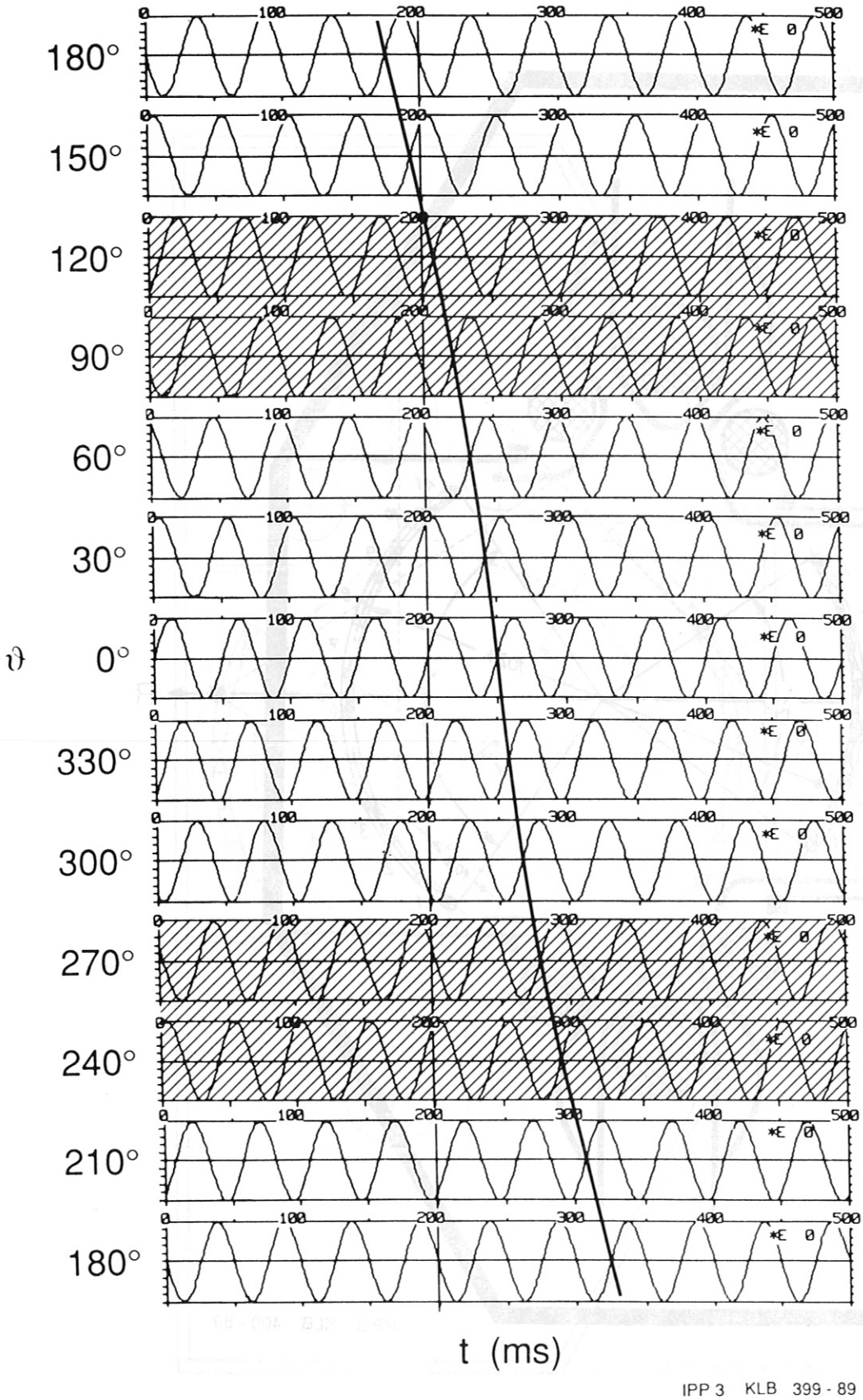

Fig. 3: Plot of $\sin\left[3\left(\vartheta - 0.4\sin\vartheta\right) + \omega t\right]$ as a function of t at various poloidal positions. $\vartheta = 0^\circ$ is in the midplane, low-field side, $\vartheta = 90^\circ$ is at the top etc. Fig 3 represents the case of equally spaced Mirnov probes; the phase can be followed easily. The case of a double-null divertor tokamak is represented by leaving out the hatched sections; the knowledge of the variation of the phase velocity is then needed for the extrapolation across the region of lacking information.

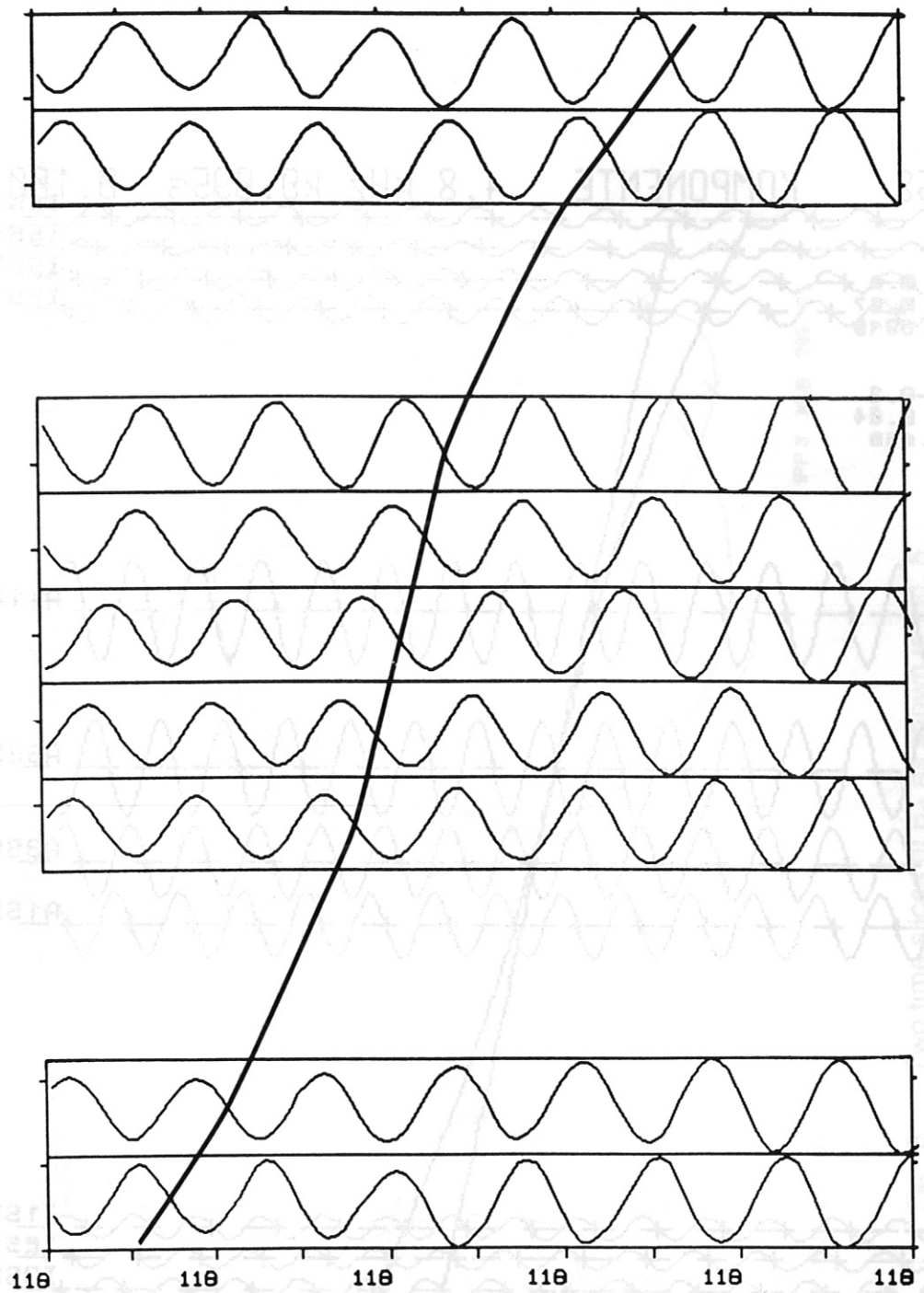

Zeitfenster : Tmin= 1.180600 Tmax= 1.181000

Zeit	Datum	Schuss	Diagn.	Signal	Massstab	Faktor	Unt	Gl	Off
12.55.02	03-MAR-88	23442	201	AMA	I4SST	0.6934	0.721E+01	51.3	0	0
12.55.02	03-MAR-88	23442	201	AMA	I7SST	1.611	0.310E+01	45.3	0	0
12.55.02	03-MAR-88	23442	201	AMA	A11SST	9.990	0.500E+00	44.5	0	0
12.55.02	03-MAR-88	23442	201	AMA	A9SST	6.855	0.729E+00	43.4	0	0
12.55.02	03-MAR-88	23442	201	AMA	A6SST	9.883	0.506E+00	44.0	0	0
12.55.02	03-MAR-88	23442	201	AMA	A3SST	4.443	0.113E+01	39.9	0	0
12.55.02	03-MAR-88	23442	201	AMA	A1SST	3.672	0.136E+01	41.1	0	0
12.55.02	03-MAR-88	23442	201	AMA	I1SST	1.191	0.420E+01	49.5	0	0
12.55.02	03-MAR-88	23442	201	AMA	I4SST	0.6934	0.721E+01	-659.8	0	0

IPP 3 KLB 398 - 89

Fig. 4: Determination of the poloidal mode number m=4 from a raw data plot of $\dot{B}_\vartheta$ according to Fig. 3. The location of the Mirnov probes can be taken from Fig. 2. The mode propagates in positive ϑ direction, i.e. from bottom to top of the plot. The figures in the column "Masstab" indicate the amplitude.

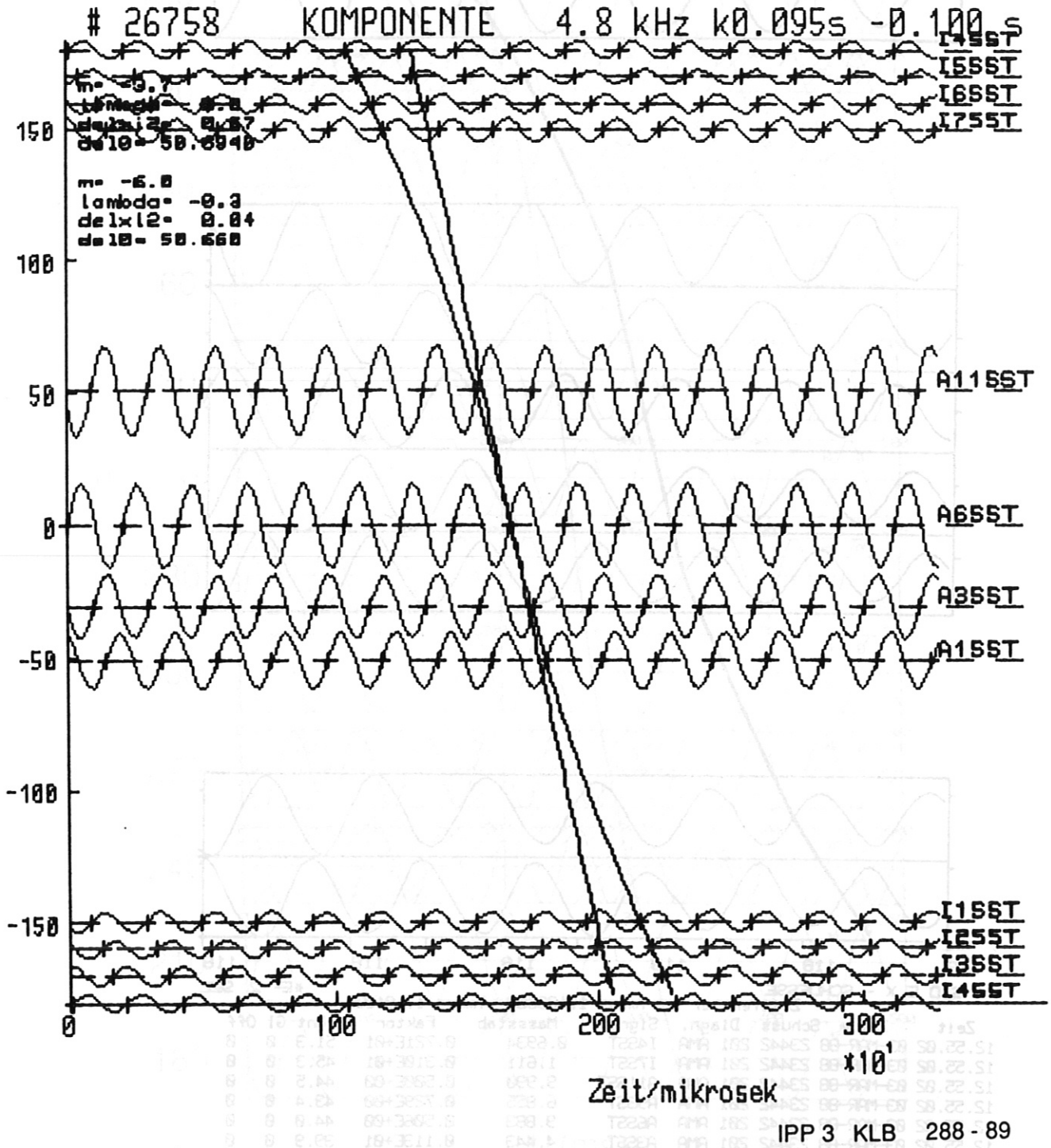

Fig. 5: Determination of the poloidal mode number m=6 from a plot of the dominant Fourier component of $\dot{B}_\vartheta$ according to Fig. 3 and a least-square fit which leads to $\chi^2 = 0.04$ while the attempt to obtain m=4 results in $\chi^2 = 0.6$.

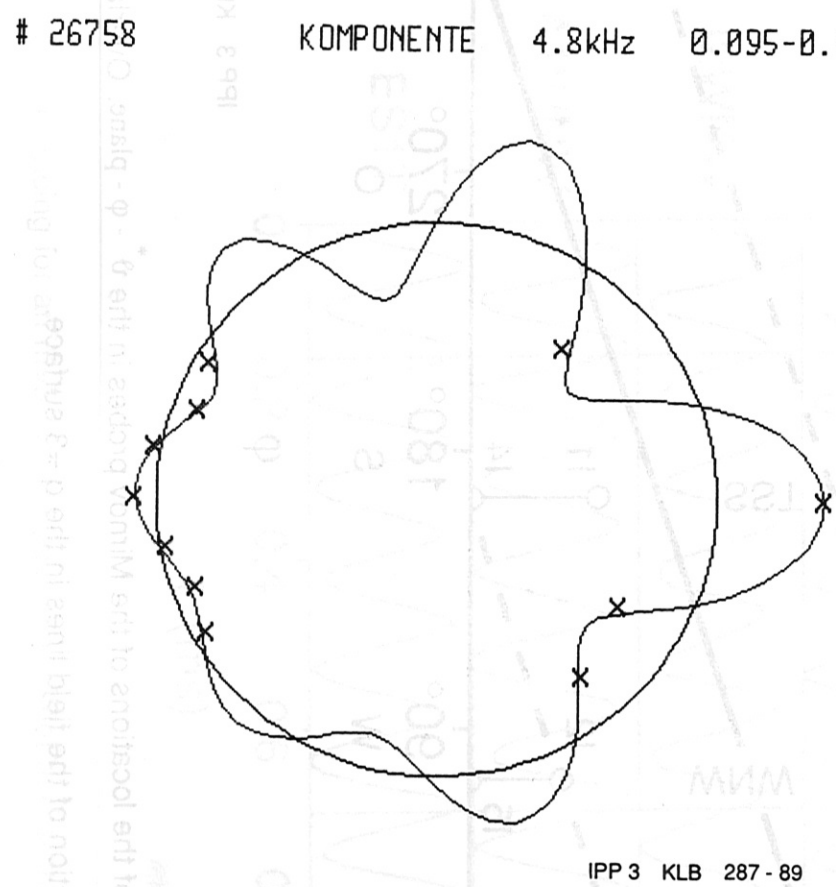

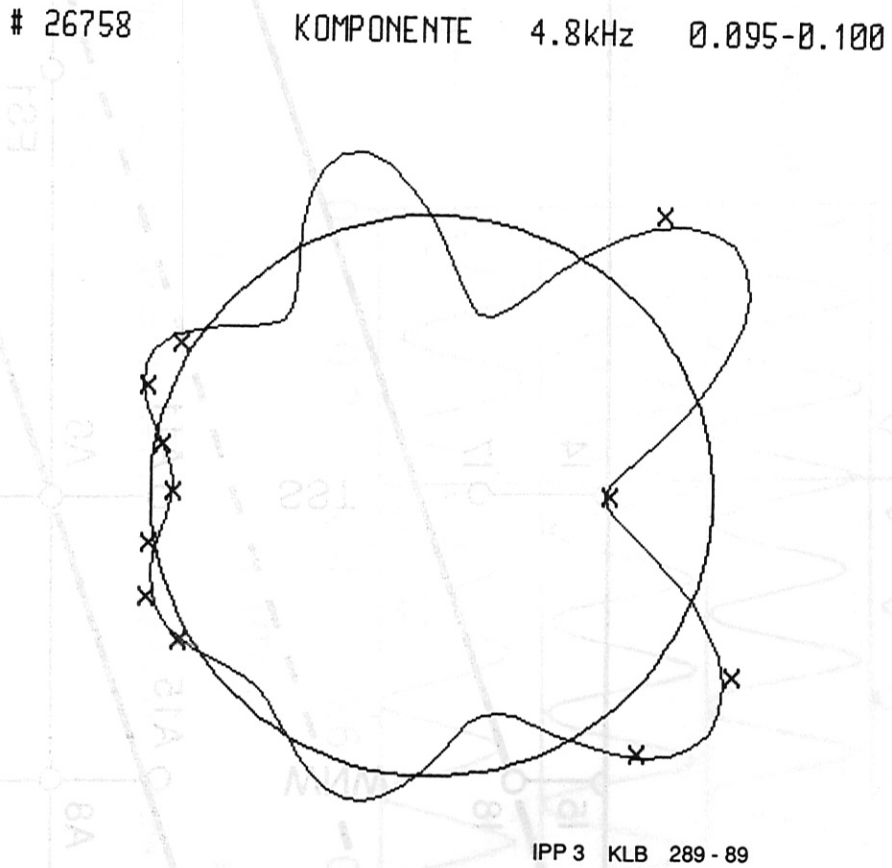

Fig. 6: Two time slices of $\dot{B}_\vartheta$ as shown in Fig. 5.

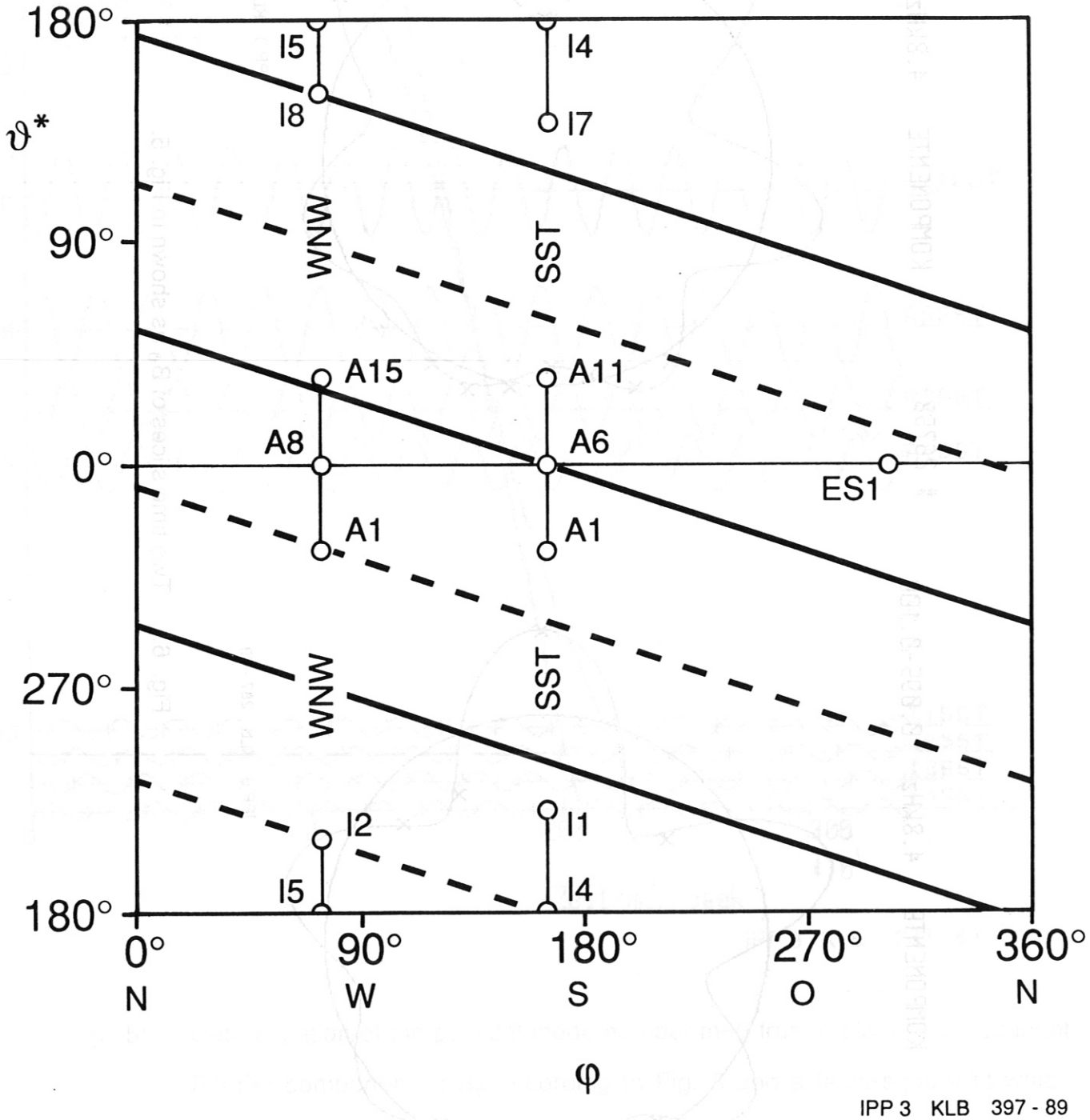

Fig. 7: Map of the locations of the Mirnov probes in the ϑ^* - φ - plane. Overlaid is the projection of the field lines in the q =3 surface.

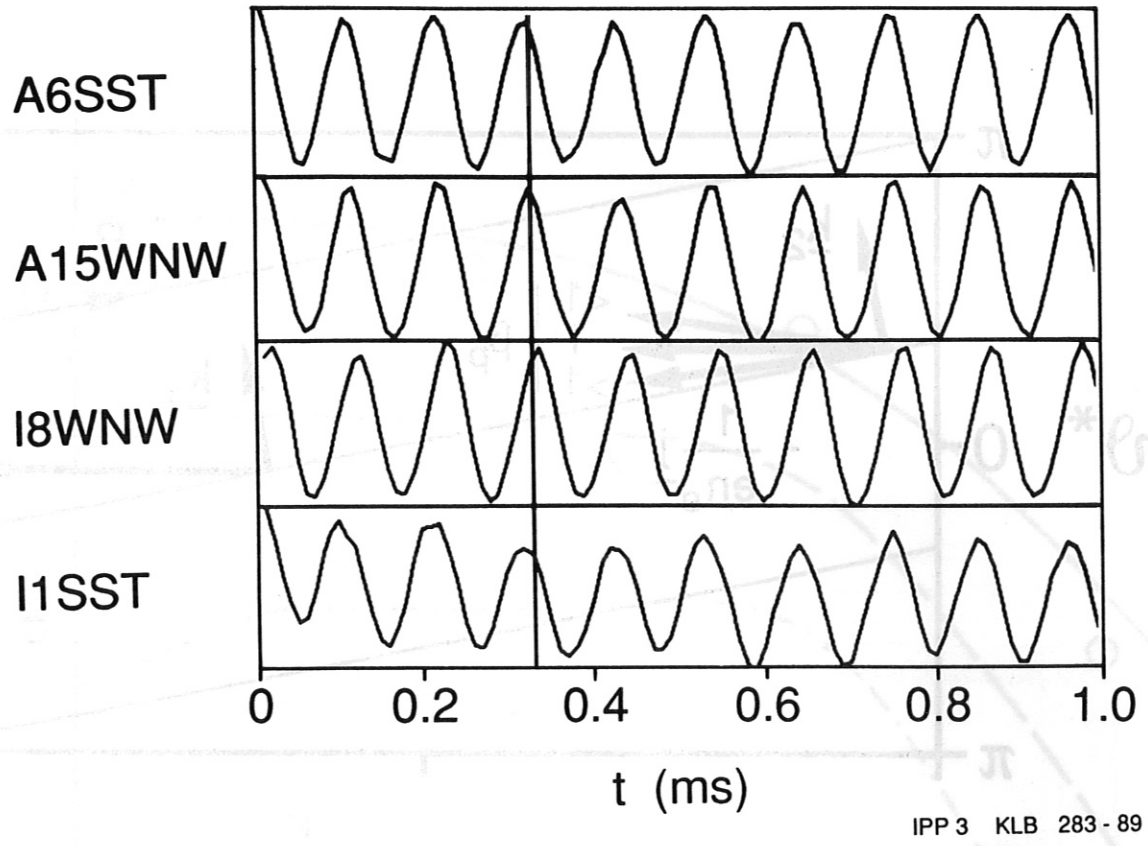

Fig. 8a: Phase tracing for an m=3 / n=1 mode. The location of the probes can be taken from fig. 7.

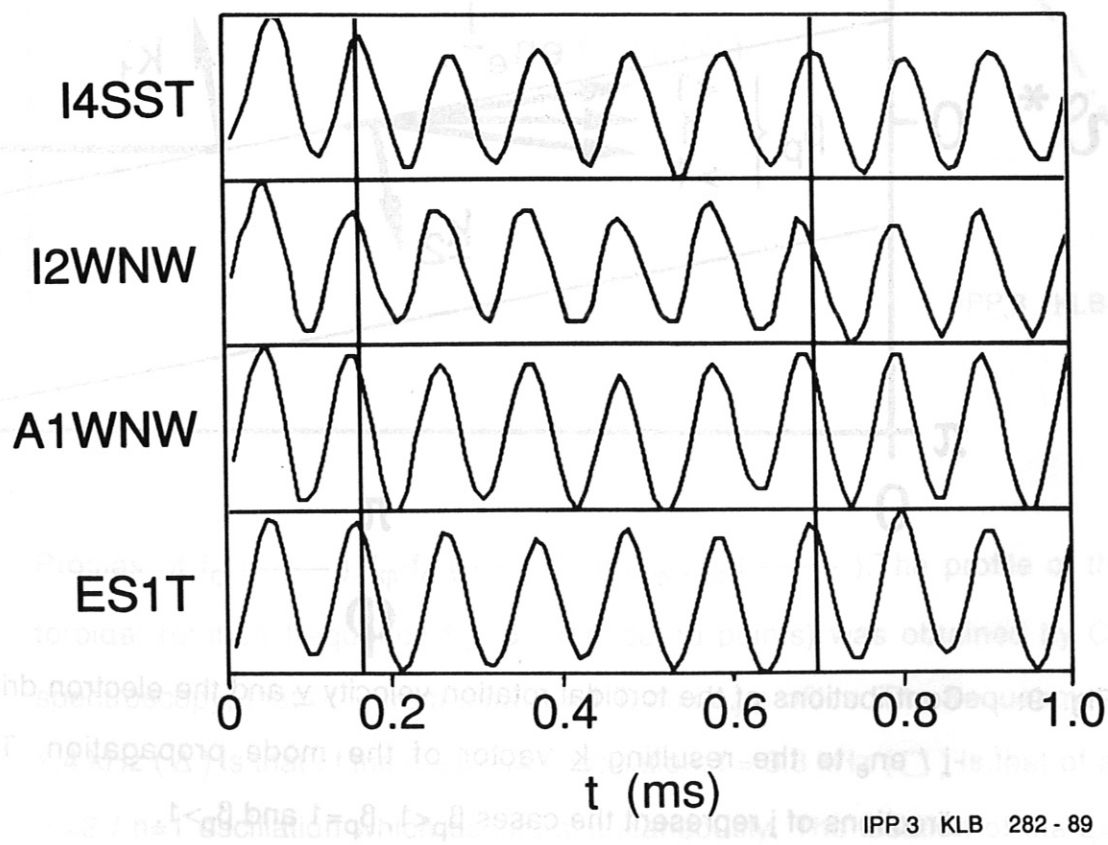

Fig. 8b: Phase tracing for an m=3 / n=1 mode; same shot and same time window as in Fig. 8a. The location of the probes can be taken from Fig. 7.

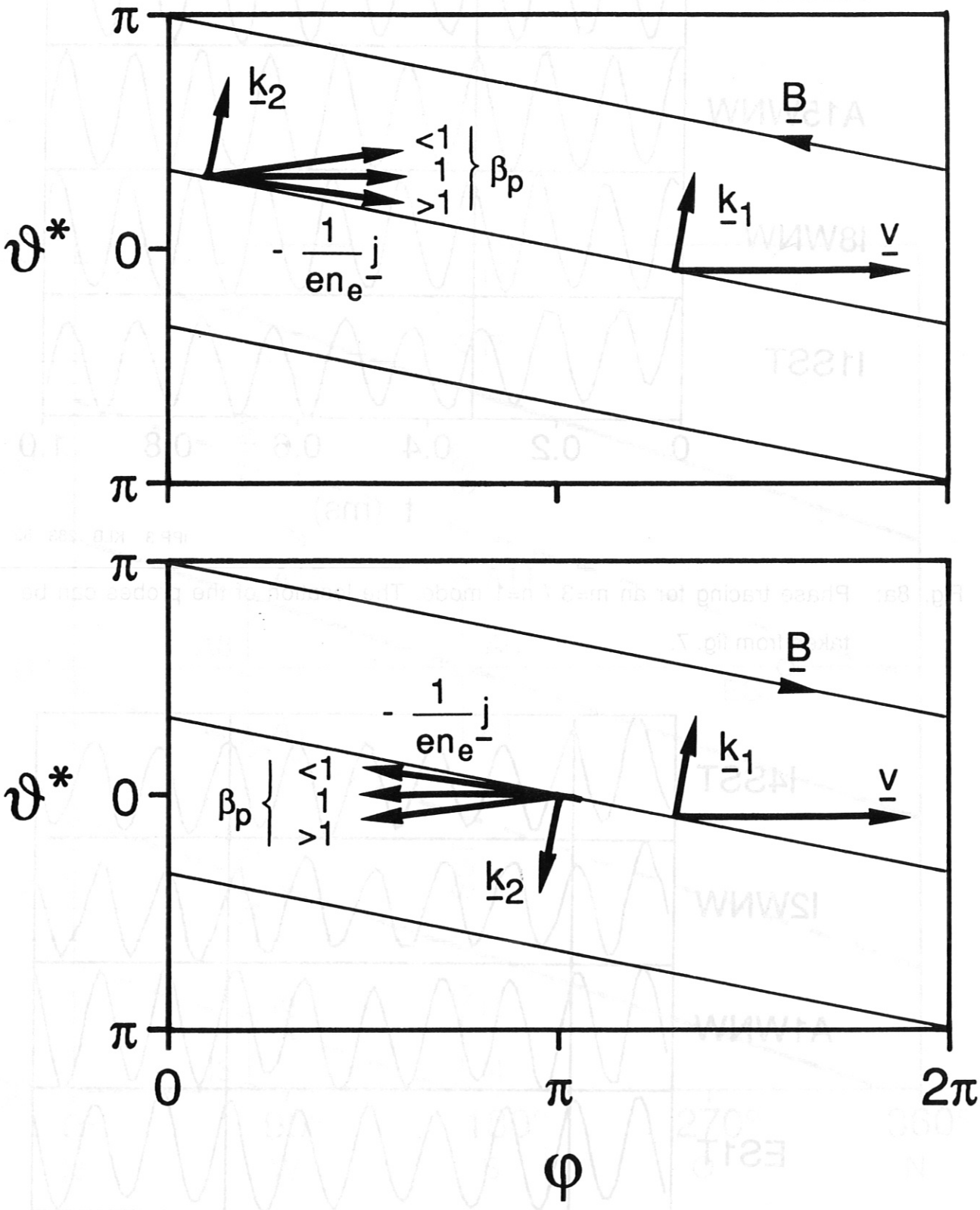

Fig. 9: Contributions of the toroidal rotation velocity $\underline{v}$ and the electron drift velocity $-\underline{j} / en_e$ to the resulting $\underline{k}$ vector of the mode propagation. The three directions of $\underline{j}$ represent the cases $\beta_p<1$, $\beta_p=1$ and $\beta_p>1$.

Top: Counter-injection.

Bottom: Co-injection. (For technical reasons, the toroidal field is reversed, too).

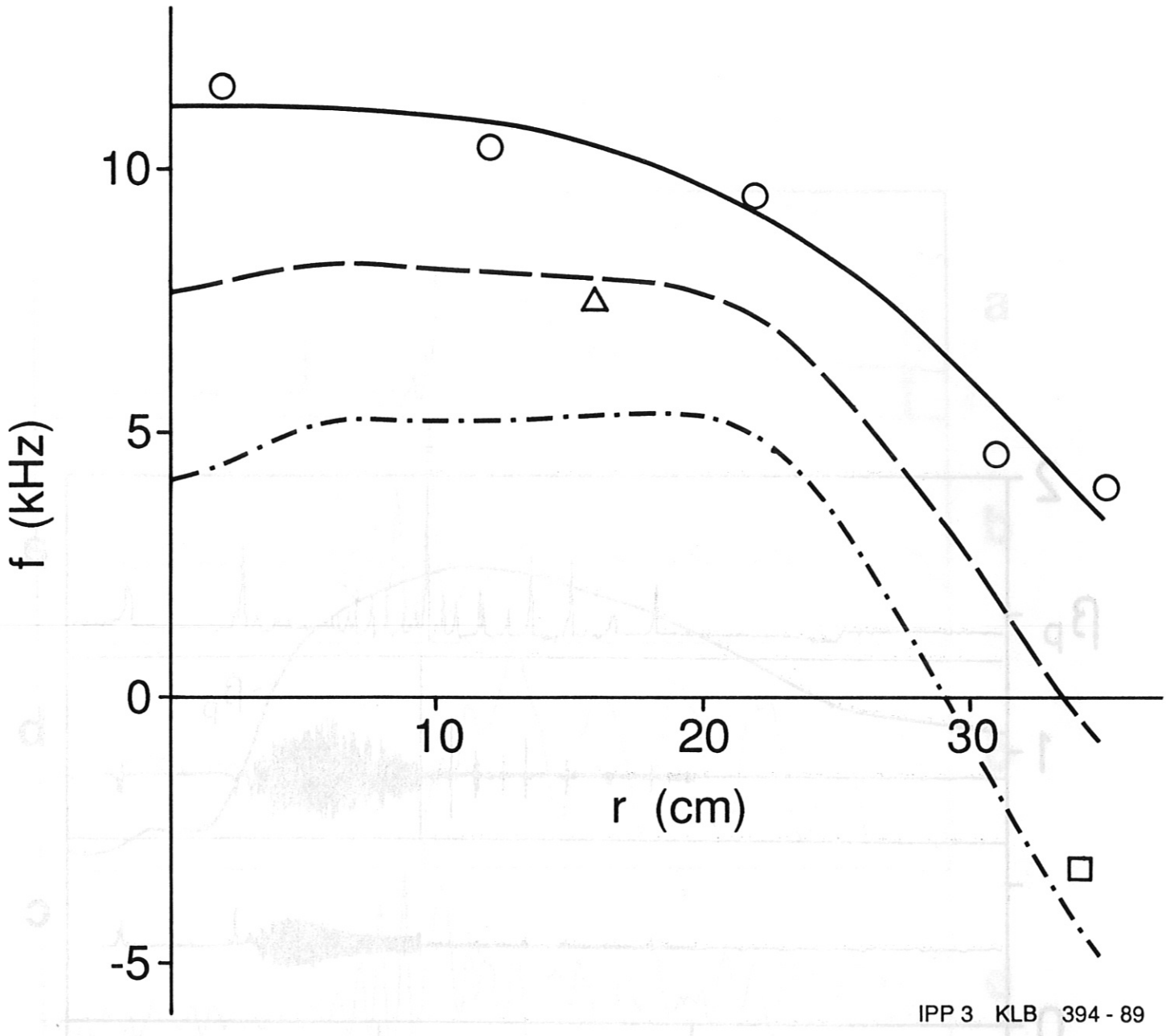

Fig. 10: Profiles of f_φ (——), $f_\varphi - f_d$ (- - - -) and $f_\varphi - 2f_d$ (- · - ·-).The profile of the toroidal rotation frequency f_φ (o - measured points) was obtained by CX spectroscopy, that of f_d from measured T_i and n_e profiles. The frequency f = 7.4 kHz (Δ) is that of the m=1 / n=1 oscillation; f = 3.3 kHz (□) is that of an m=2 / n=1 oscillation which occurs simultaneously. The location of the q=1 surface is obtained from SX measurements, that of the q=2 surface is estimated.

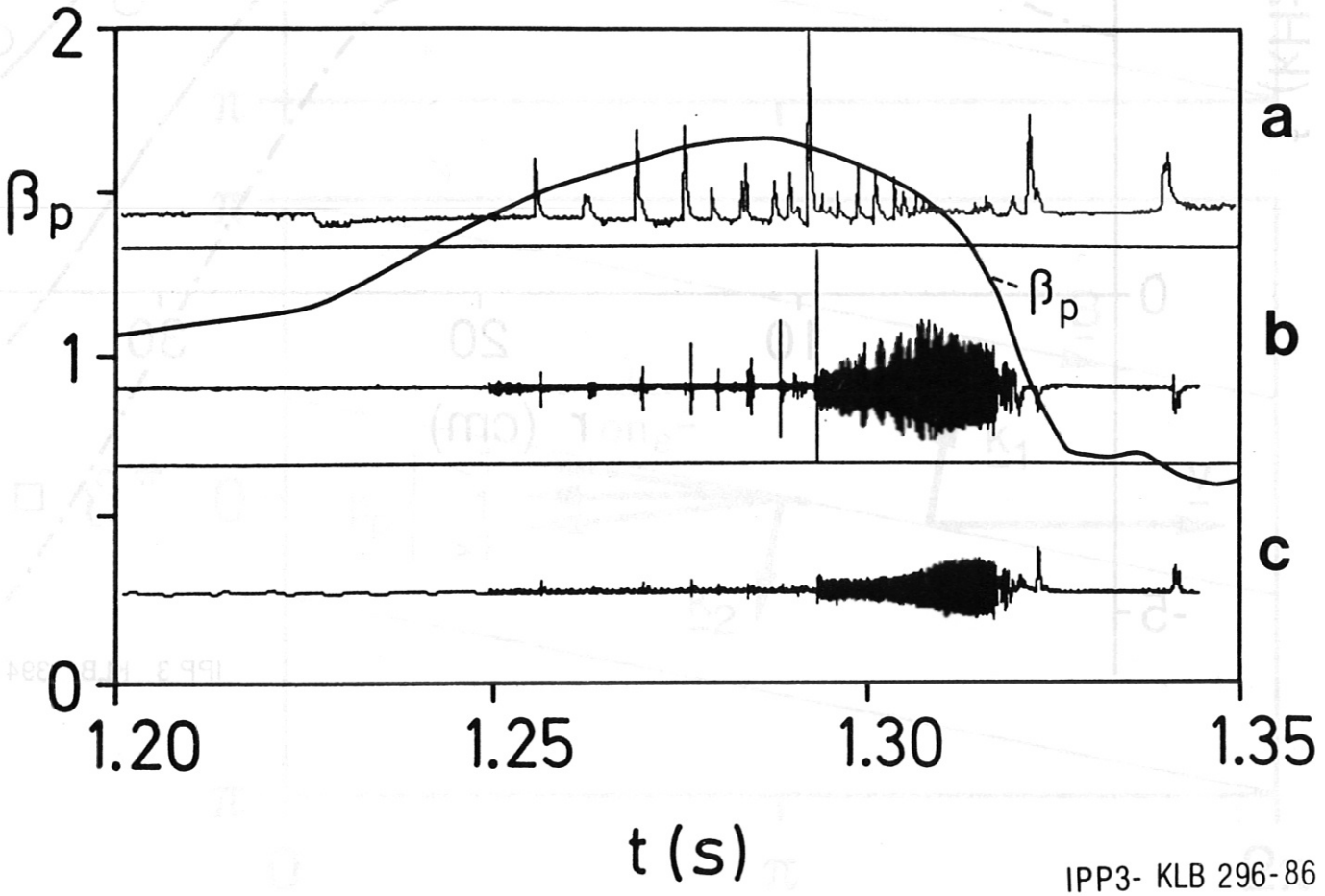

Fig. 11: MHD activity of a H-type plasma approaching the Troyon beta limit. Trace a: H_α / D_α emission from a divertor chamber indicating the occurrence of ELMs. Trace b: $\dot{B}_\vartheta$ signal from a Mirnov probe located in the midplane at the low-field side. Data acquisition starts at t = 1.25 s. Trace c: Same from the high-field side. Overlaid is the temporal evolution of the poloidal beta.

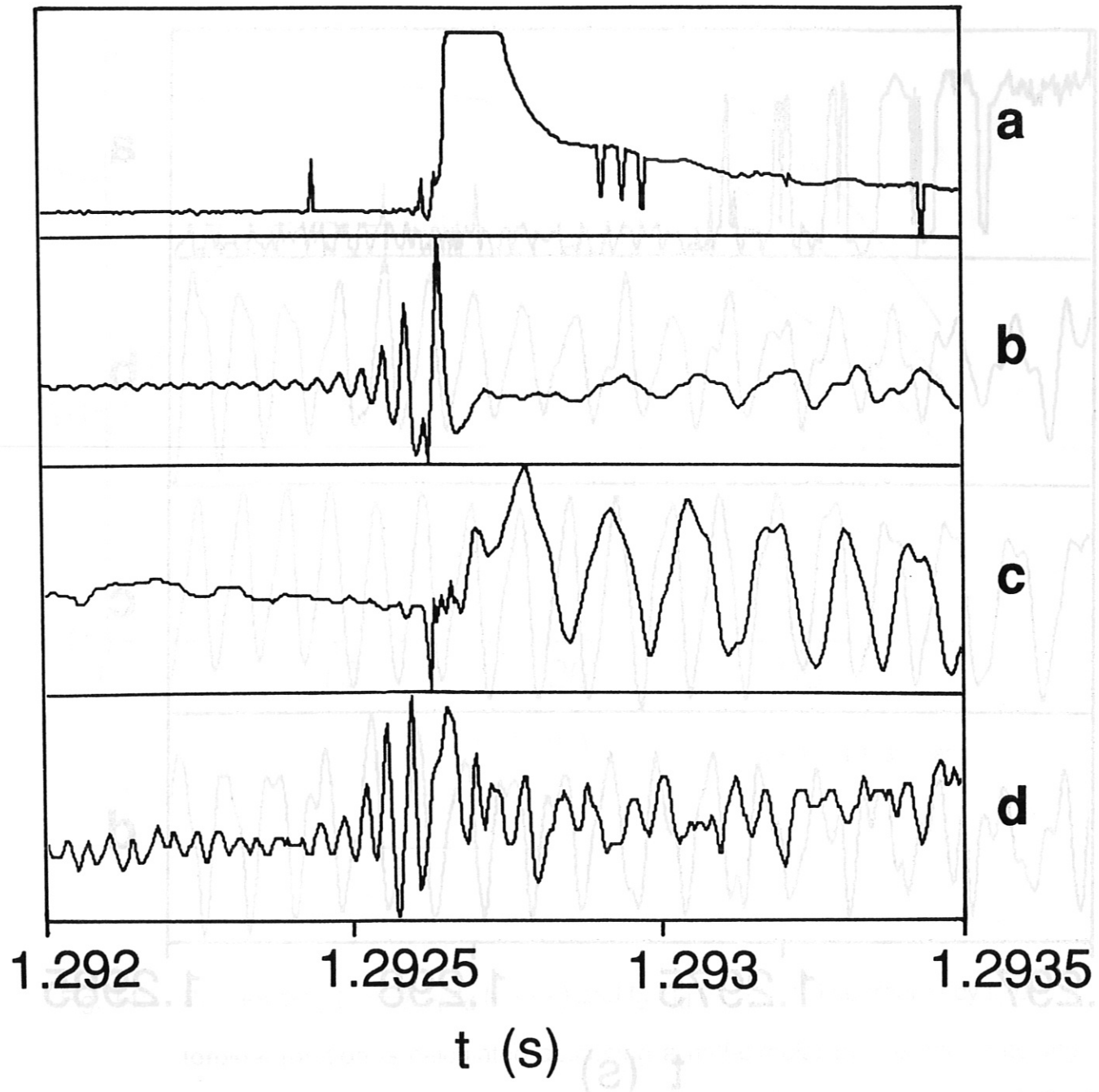

IPP 3 KLB 405 - 89

Fig. 12: Expansion of Fig. 11. Trace a: H_α / D_α emisssion. (The signal of the photodiode saturates.) Trace b: $\dot{B}_\vartheta$, midplane outside. Trace c: $\dot{B}_\vartheta$, midplane inside. Trace d: SX diode signal from a near-centre chord.

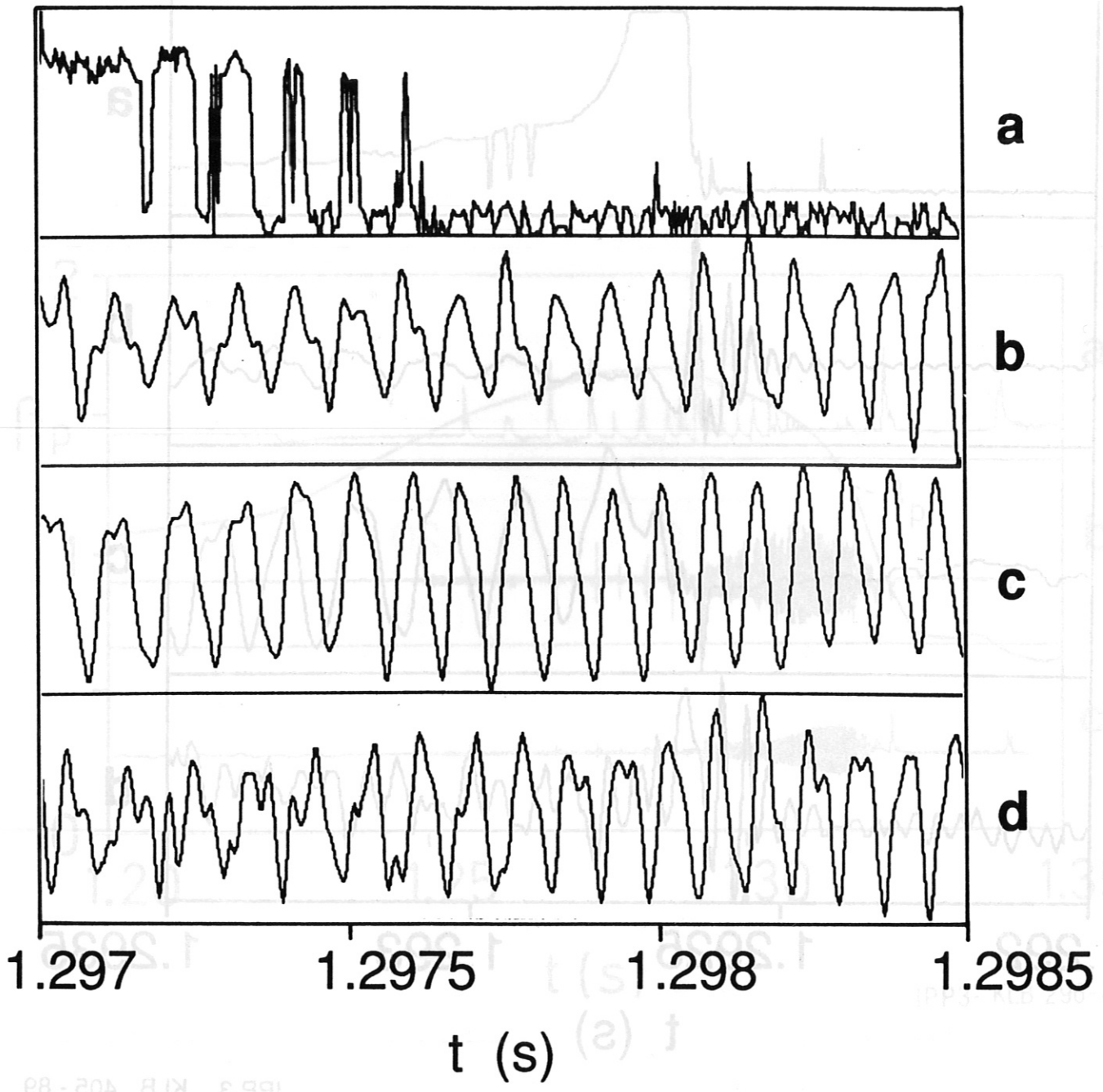

IPP 3 KLB 404 - 89

Fig. 13: Expansion of Fig. 11. Same traces as in Fig. 12, 5 ms later. Note that the mode frequency is transiently seen in the H_α / D_α signal, too.

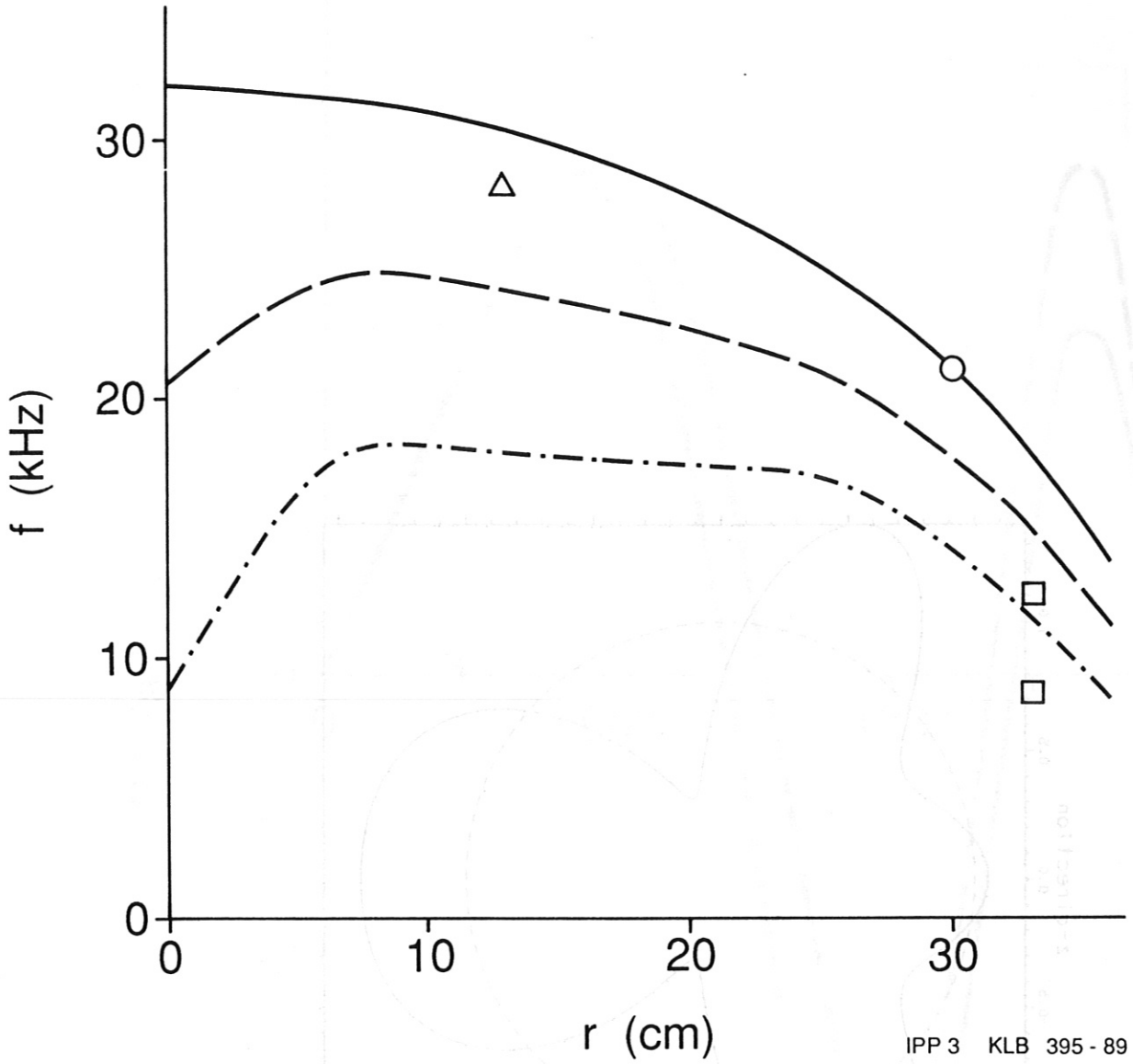

Fig. 14: Profiles of f_φ (——), f_φ-f_d (- - - -) and f_φ-$2f_d$ (- · - · -). The frequency f_φ of the toroidal rotation is calculated assuming a half-circular profile and matching the measured value at r=30 cm (o). The frequency f_d due to the diamagnetic drift was obtained from measured T_i and n_e profiles. f = 28 kHz (Δ) is the frequency of the m=1 / n=1 oscillation (cf. Fig. 12). f = 8.5 kHz and f = 12.6 kHz (□) are the frequencies of the m=2 / n=1 oscillation (cf. Figs. 12 and 13). The location of the rational surfaces q=1 and q=2 were obtained from a code simulation.

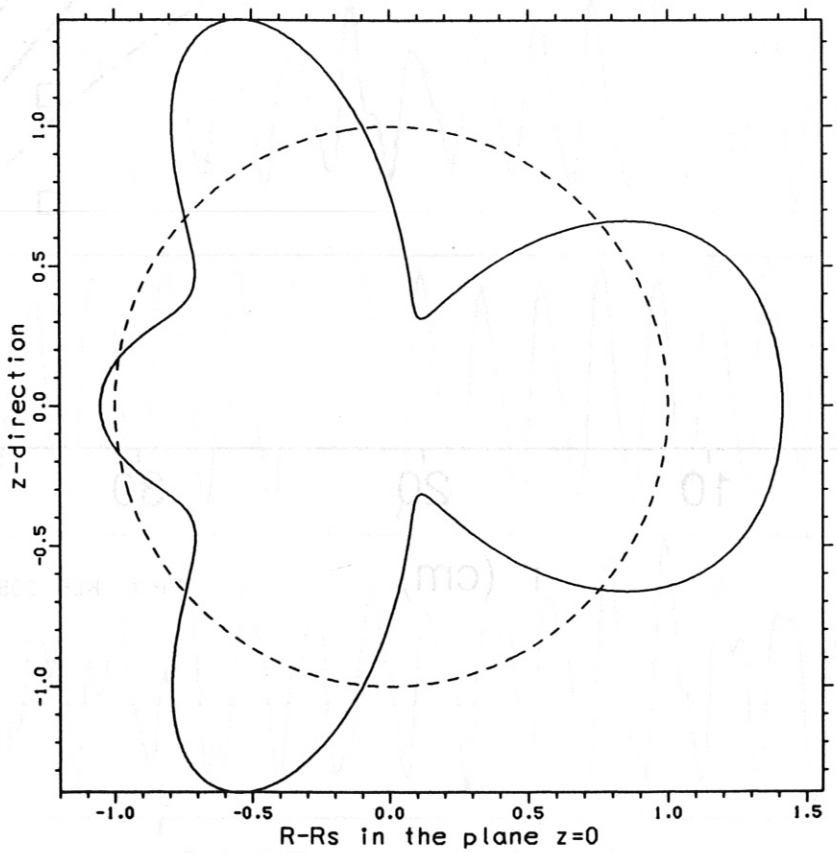

Fig. 15: Polar diagram of the field perturbation $\tilde{B}_\vartheta$ calculated according to the model of Fussmann, Green and Zehrfeld for $\beta_p = 1.5$.

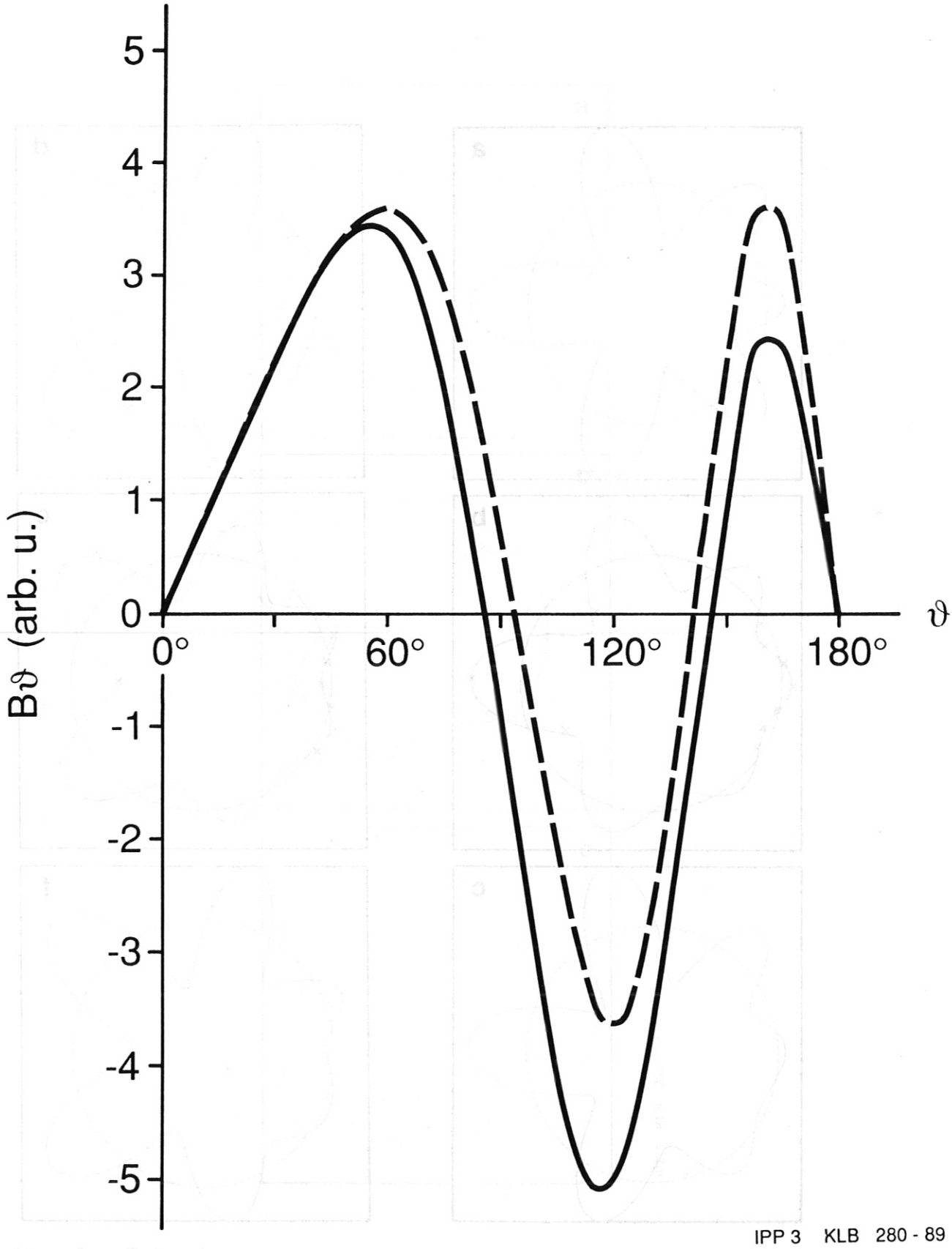

Fig. 16: Poloidal variation of wavelength and amplitude for m=3. Solid line: Calculation according to the model of Fussmann, Green and Zehrfeld. Dashed line: B_ϑ = const. sin [3 (ϑ - 0.62 sin ϑ)], according to Merezhkin´s transformation.

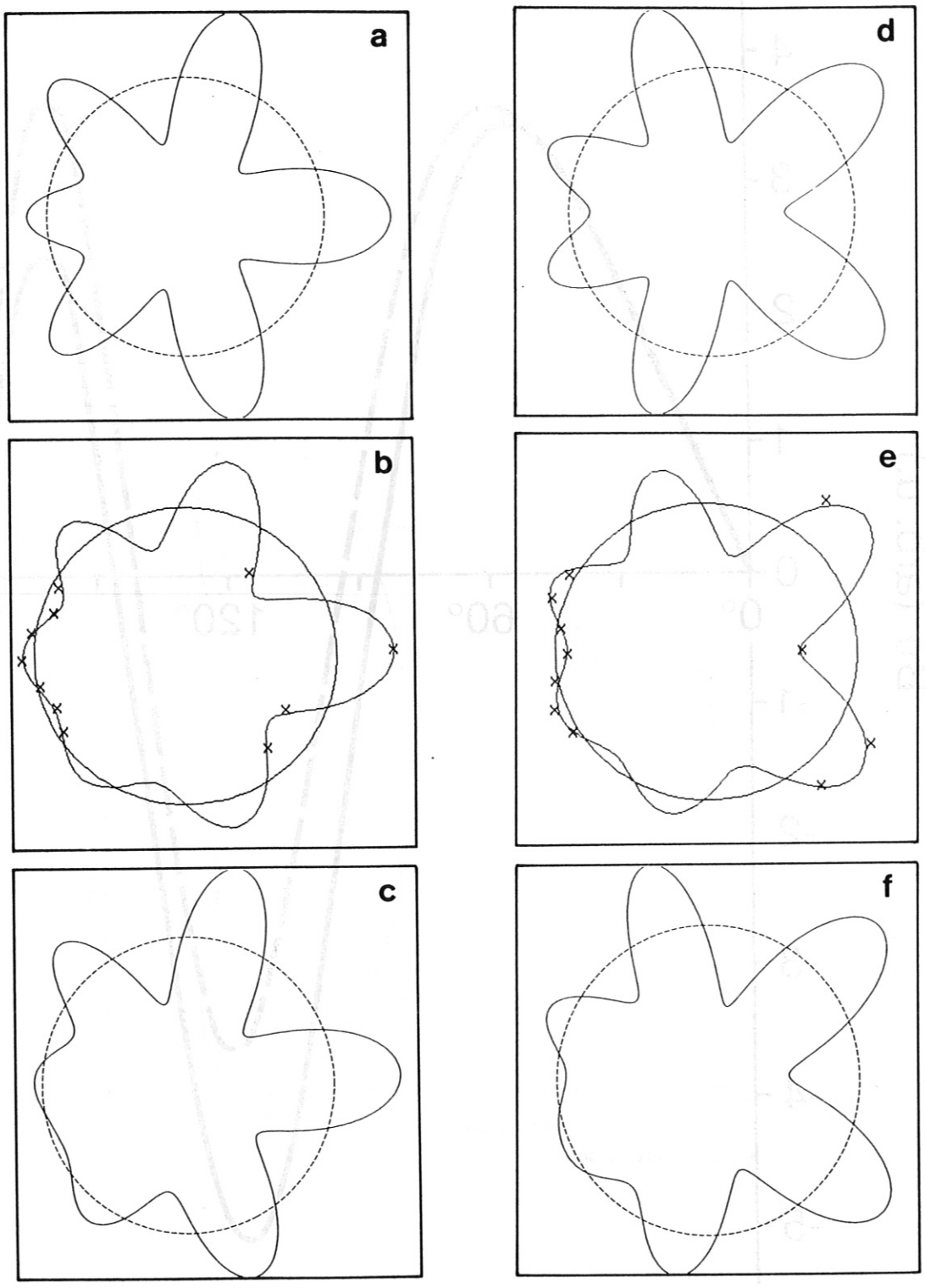

Fig. 17: Simulation of a measured m = 6 structure by the model of Fussmann, Green and Zehrfeld. Figs. 17b and 17e are identical with the polar plots of Fig. 6. The leading m = 6 component of the simulation is shown in Figs. 17a and 17d. The polar plots of Figs. 17c and 17f are obtained by adding the m = 5 and m = 7 sidebands with a relative amplitude of 0.2 and a phase shift of $\pm$ 23°.

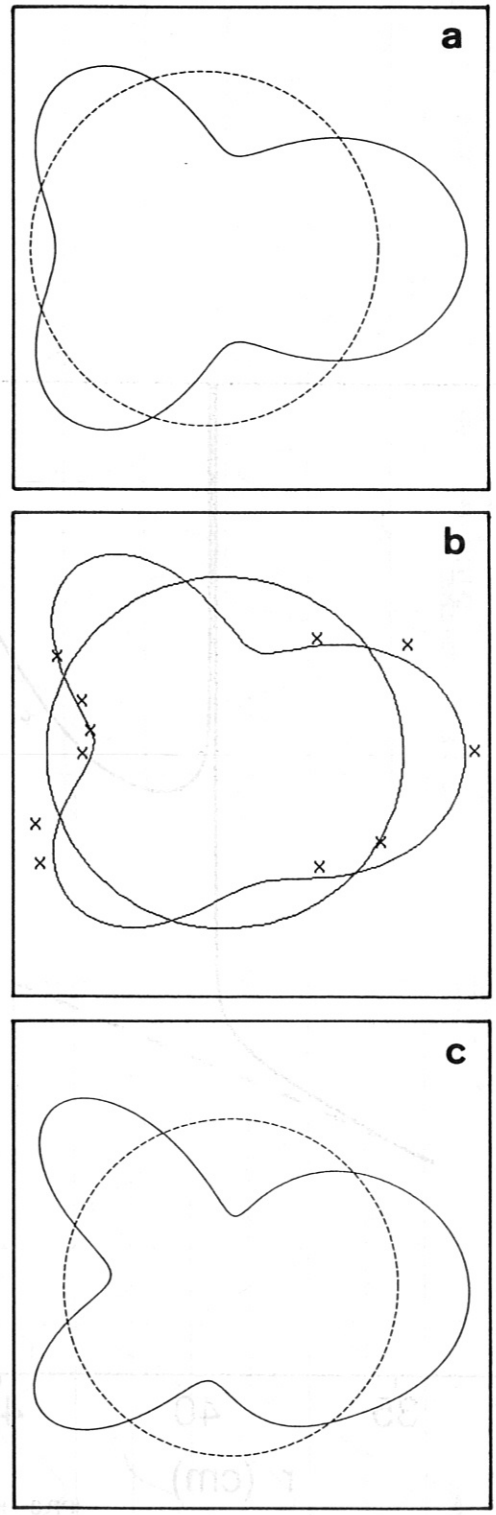

Fig. 18: Polar diagrams of the field perturbation $\tilde{B}_\vartheta$ according to measured data (Fig. 18b) and simulations. Fig. 18a shows the leading component, Fig. 18c a simulation with sideband amplitudes of - 0.22 and a phase shift of $\pm$ 8°.

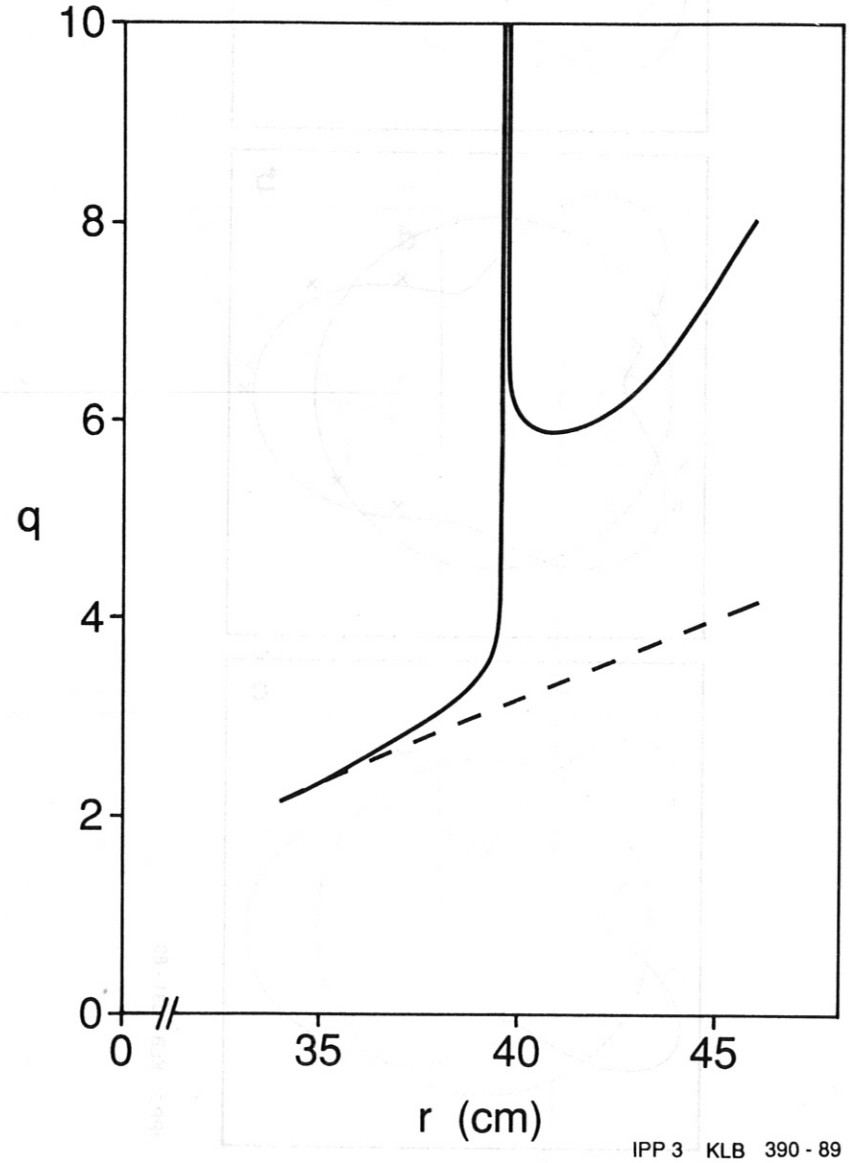

Fig. 19: q profile in the midplane of a divertor (solid line) and of a limiter tokamak.

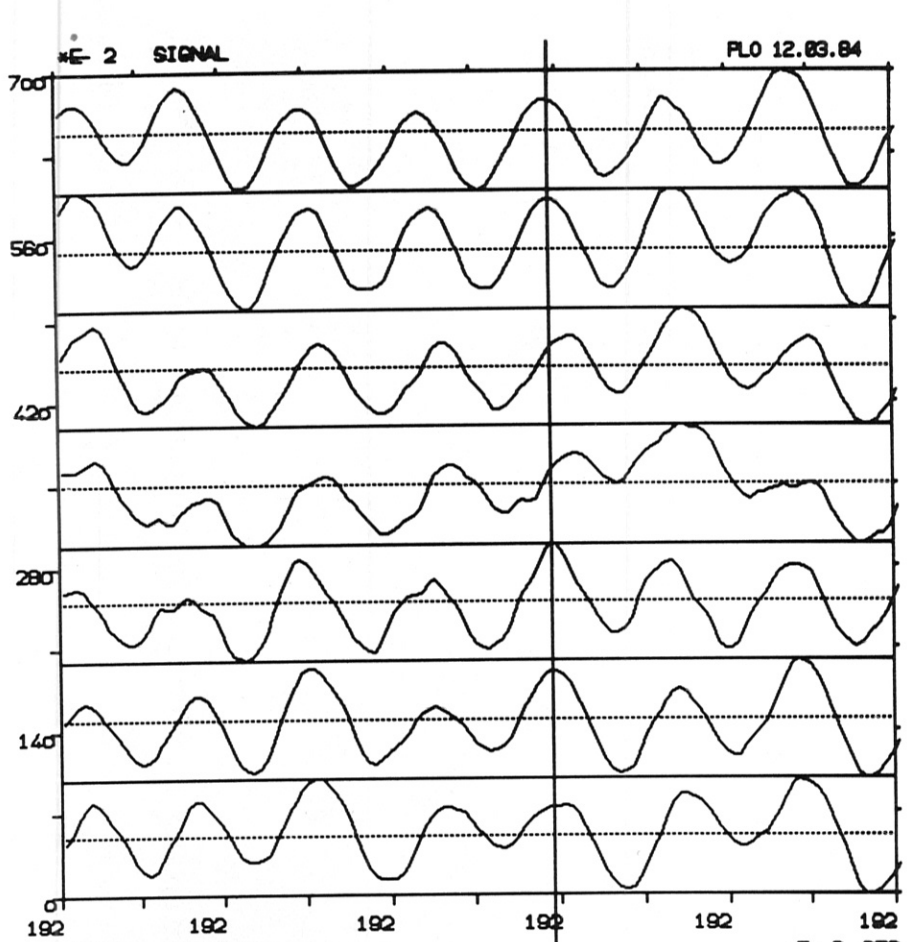

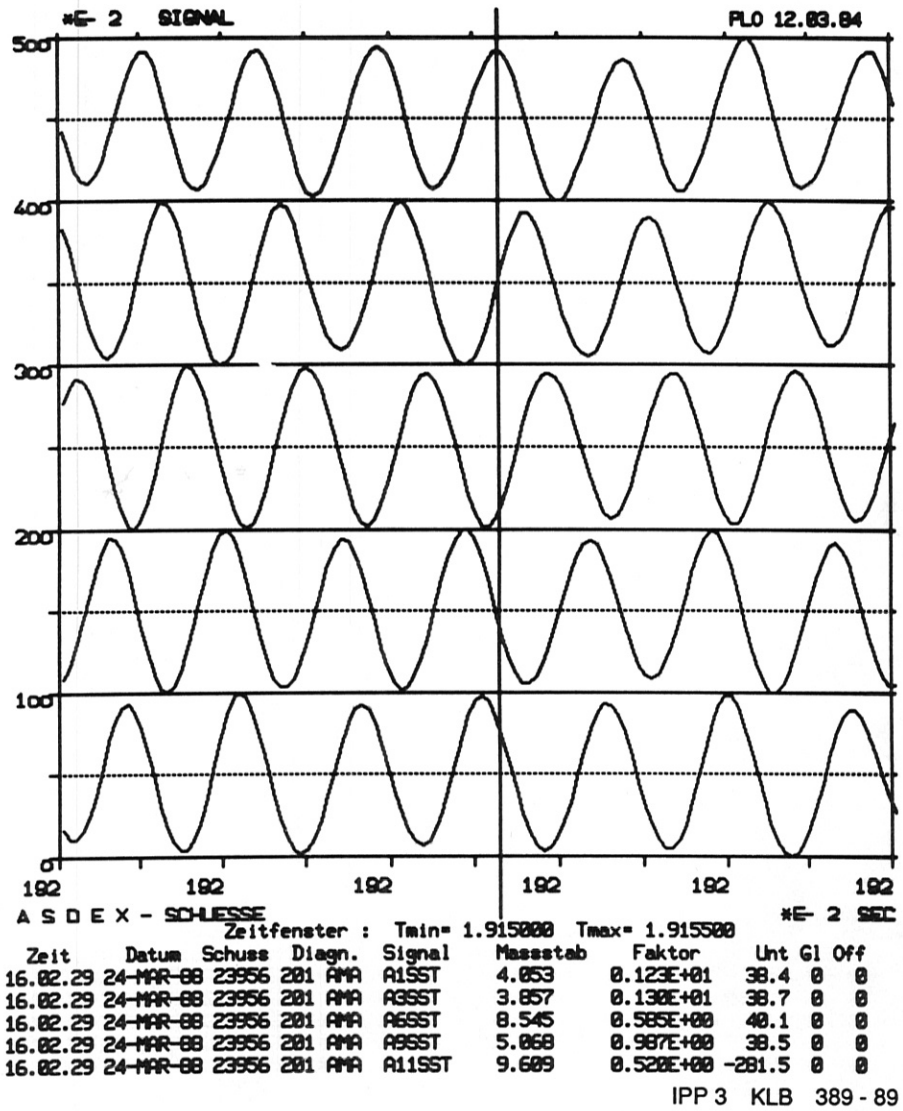

Fig. 20: $\dot{B}_\vartheta$ traces from Mirnov probes located at the high-field side (left) and at the low-field side (right) of the torus. The location of the probes can be taken from Fig. 2. Superposition of an m = 0 and an m = 4 mode.